

Evidence on a Class of Azimuthally Propagating Dipolarization Structures in the Earth's Magnetosphere from 4 to 30 Re

S. Tian¹, C. A. Cattell¹, J. R. Wygant¹, V. Angelopoulos², and G. D. Reeves³

¹School of Physics and Astronomy, University of Minnesota, Minneapolis, Minnesota, United States

²Institute of Geophysics and Planetary Physics, University of California, Los Angeles, California, United States

³Los Alamos National Laboratory, Los Alamos, New Mexico, United States

Key Points:

- A class of dipolarizations propagate azimuthally at 3 deg/min, or 50 km/s at 6.6 Re
- The azimuthally propagating dipolarizations (APDs) are finger-like: ~ 2 Re wide and up to 20 Re long
- APDs often propagate away from midnight, sweep over 3-6 hours in local time in 20-30 min

Abstract

We report observational evidence for a class of coherent magnetic dipolarization structures that are long lived and radially extensive. The reported dipolarization structures, a subset of general dipolarizations, typically remain coherent over 20-30 min in real time, 3-6 hours in MLT, and 10-20 Re in radial distance. Arrays of more than three spacecraft in non-collinear geometry are used to determine the propagation vector, including both the normal speed and direction, of such dipolarizations in the equatorial plane. The determined azimuthal propagation is ~ 3 deg/min, which corresponds to ~ 50 km/s at 6.6 Re. This speed is consistent with those obtained from two azimuthally separated spacecraft in previous works. Further analysis suggests that these azimuthally propagating dipolarizations (APDs) are often finger-like in shape, ranging from 5 to 20 Re in length and several Re in width. The reported APD may accompany the earthward flow channel and dipolarizing flux bundle (DFB).

1 Introduction

Dipolarization describes the sudden change of the Earth's magnetic field from a stretched to dipole configuration. Consequently, the accepted observational signature of a dipolarization is the sudden increase of the poloidal tilt angle of the magnetic field (Nagai, 1982; Ohtani et al., 2018). Since early observations (Cummings et al., 1968), dipolarization has been a focus of attention because it plays a central role in the energy release in the Earth's magnetotail (Lui, 1996; Angelopoulos et al., 2008). It has been extensively studied from the MHD (magnetohydrodynamic) scale down to kinetic scales (Fu et al., 2020, and references therein). In this paper, we focus on the spatial evolution of dipolarizations and determine the propagation speed and direction and related MHD scale properties. Such information is crucial in understanding how dipolarization couples the Earth's magnetosphere and ionosphere.

Ohtani et al. (2018) studied the azimuthal evolution of dipolarizations within and around 6.6 Re using the technique of 2-spacecraft timing on the tilt angle data. The authors found that, statistically, the azimuthal phase speed of the propagation is 30-50 km/s and divergent around midnight. The phase speed and divergent pattern are consistent with an earlier study at 6.6 Re (Nagai, 1982). However, due to the limitations of 2-spacecraft timing, the full propagation vector has not yet been examined. For example, in Figure 1, the phase speed along the line connecting spacecraft 1 and 2 is

$$|\vec{v}_{1,2}| = |\vec{v}_n| / (\hat{v}_n \cdot \hat{s}_{1,2}), \quad (1)$$

which is often larger than the normal speed $|\vec{v}_n|$. This argument also applies for any number of co-linear spacecraft. In this paper, we extend the earlier studies by adopting the technique of 3-spacecraft timing to explicitly determine the full propagation vector and by studying a broader region from 4 to 30 Re.

Two dipolarization related structures have been proposed and extensively studied beyond 6.6 Re. A dipolarizing flux bundle (DFB) or dipolarization front is a 3D flux tube (Liu et al., 2013, 2014), which has an equatorial cross section of about 2 Re wide and long (c.f. Figure 10). In addition, both smaller (0.3 Re, (Nakamura et al., 2002)) and larger (3-4 Re, (Huang et al., 2015)) azimuthal widths have been reported in case studies. A DFB probably propagates earthward because timing around midnight shows that its earthward phase speed is about 300-500 km/s (Runov et al., 2009, 2011) and because DFBs are typically accompanied by earthward bursty bulk flows (BBFs) (Baumjohann et al., 1990; Angelopoulos et al., 1992) at a similar speed. However, a Cluster study shows that earthward BBFs may also be observed with an azimuthally propagating dipolarization front (Nakamura et al., 2002). The second type is related

to the azimuthal and tailward expansion of the dipolarized region (Baumjohann et al., 1999; Nakamura et al., 2011). The proposed explanation is the pileup of magnetic flux due to the earthward BBFs and DFBs. This explanation is supported by tail observations and MHD simulations (Sigsbee et al., 2005; Birn et al., 2019; Merkin et al., 2019). In Section 5, we will discuss the relation between the azimuthally propagating dipolarizations reported herein to these two types of dipolarizations structures.

In this paper, we describe a statistical study of the propagation direction and speed of dipolarizations in the equatorial plane from 4 to 30 Re. We search for events when >3 spacecraft observe similar dipolarization signatures, so that the propagation vector can be robustly determined using multiple combinations of 3 non-collinear spacecraft. Using this propagation velocity, other important properties can be determined, including the azimuthal width, radial extent, life-time, and propagation extent. We report evidence for a class of dipolarizations which propagate azimuthally and extend well beyond geosynchronous orbit, reaching to 30 Re in some events. The observed properties suggest a new scenario for how dipolarizations propagate in the magnetotail. A discussion on the limitations of our dataset is also included.

2 Instrumentation

The primary data set to analyze dipolarizations is the DC magnetic field. There are 11 spacecraft available in the region of interest with a DC magnetometer, including the 2 Van Allen Probes (RBA/B) launched in 2012 (Kletzing et al., 2013), the 5 THEMIS spacecraft (THA/B/C/D/E) launched in 2007 (Auster et al., 2008), the 3 GOES spacecraft (G13/14/15) launched in 2006-2010 (Singer et al., 1996), and the 4 MMS spacecraft launched in 2015 (Torbert et al., 2016). Only MMS1 is used since the MMS separations are too small for definitive timing. All magnetic field data are down-sampled to a common cadence of 10 sec, to facilitate a uniform treatment in later calculations.

The apogees of the spacecraft we use are at 5.8 Re, 6.6 Re (circular orbit), and beyond 10 Re for the RBSP, GOES, and THEMIS/MMS missions, respectively. As a result of the apogee separation, the spacecraft utilized for each event cover a large area of the equatorial plane, typically on the order of 3-6 hr in MLT \times 5-20 Re in R_{xy} . These spacecraft can be off the magnetic equator by ~ 20 deg due to the wobble of the earth's dipole axis. We will show that this z-separation from the magnetic equator introduces a significant error in timing along the radial direction but not in the azimuthal direction. We define the error δMLT and δR_{xy} as the difference between the in-situ position of a spacecraft and its equatorial footprint in MLT and R_{xy} respectively. For all the dipolarizations studied in this paper, δR_{xy} is 1.5 Re on average. Its standard deviation is 2.5 Re and its maximum absolute value is 16 Re. These results show that the error in R_{xy} due to the z-separation is comparable to the typical range in radial distance (5-20 Re) and thus the error is significant. These results are based on the mapping with the T89 model but other models provide essentially the same results. Similarly, δMLT is 0.02 hr on average. Its standard deviation is 0.08 hr and its maximum absolute value is 0.4 hr. These results are much smaller than the range in MLT (3-6 hr) and thus the error due to the z-separation in azimuthal timing is negligible. Therefore, we primarily study the azimuthal propagation of dipolarizations with this dataset. Throughout our paper, we use the in-situ positions to perform timing because they do not include the possible errors associated with the equatorial footprints. The reported dipolarization structures would be more radially extensive if the equatorial footprints were used (Apatenkov et al., 2007).

3 Example Events

Figure 2 shows a dipolarization event on August 28, 2014 when an individual dipolarization was observed by 6 spacecraft. The left hand panels show the detrended tilt angle θ of the measured magnetic field at each satellite. The dipolarization, seen as the ramp of increasing θ , lasted for 5-10 min at each satellite while remaining coherent for over ~ 30 min. The spacecraft were distributed in the post-midnight sector over 6 hours in MLT and from 5 to 12 Re (Figure 3f). As discussed in Appendix A, for each dipolarization, we determine its major properties including the duration ΔT , the net tilt angle change $\Delta\theta$, and the “ramp time” (the center time of the ramp). Appendix A also presents the method used to remove background magnetic field changes and identify dipolarizations. The right hand panels in Figure 2 show the θ data are aligned based on the ramp time. The time lag of the ramp times is consistent with results from cross-correlation, as presented in Appendix B and Figure 13. Several interesting features can be seen in Figure 2. The dipolarization remained coherent for ~ 30 min. The change of tilt angle was about 40-50 deg near local midnight (panel a-1 and a-2), about 30 deg around 2 MLT (panel a-4), and below 10 deg around dawn (panel a-5 and a-6), suggesting an azimuthal decay of $\Delta\theta$ in MLT. Similar characteristics are seen in the other events in this section and the larger data set described in Section 4.

Figure 3 displays how we determine the dipolarization propagation and the relevant properties. To relate the time and location of the dipolarization observations, the detrended tilt angle θ in Figure 2 are re-plotted in Figure 3c and 3d, color-coded along the spacecraft tracks in MLT and x_{SM} respectively. Panel 3b uses the same color-coding to show the data for 16 hours around the event in panel 3c and 3d. The longer period was during the recovery phase of a geomagnetic storm and contained two large substorms when AE exceeded 1000 nT (Figure 3a). In Figure 3b, several examples are marked when dipolarizations were seen to “drift” in MLT away from midnight. Such drifts in MLT were very common during this and other storms/substorms.

Figure 3f shows the propagation velocity \vec{v}_n determined from 3-spacecraft timing. In the equatorial plane (Figure 1), we have

$$\begin{aligned} (\vec{r}_1 - \vec{r}_2) \cdot \hat{v}_n &= |\vec{v}_n|(t_1 - t_2) \\ (\vec{r}_1 - \vec{r}_3) \cdot \hat{v}_n &= |\vec{v}_n|(t_1 - t_3), \end{aligned} \quad (2)$$

where $t_{1,2,3}$ is the ramp time of the dipolarization at spacecraft 1, 2, and 3 and $\vec{r}_{1,2,3}$ is the corresponding location. This is a linear equation in $\hat{v}_n/|\vec{v}_n|$, which is solvable when 1, 2, and 3 are non-collinear and when the time lags are well determined. \vec{v}_n is then obtained from $\hat{v}_n/|\vec{v}_n|$. Non-collinearity requires that a triangle formed by the 3 spacecraft cannot be too acute or obtuse. We require that triangles to have all angles within 15 and 165 deg. Figure 3f shows an example of a triangle of good geometry in the August 28, 2014 event, and Figure 4e shows all triangle combinations of both good and bad geometries for a different event. In addition, we use the ramp times to calculate the time lag between any two spacecraft. For the purpose of error control, time lags are independently determined from cross-correlation. The \vec{v}_n vectors of a certain triangle calculated from the two methods are required to be consistent: the difference in magnitudes $< 20\%$ and in directions < 30 deg. In this study, we define a “triad” as a triangle when both the geometry and timing criteria are satisfied.

In the August 28, 2014 event, there are 20 (C_6^3) possible triangles. Applying the above criteria results in 13 triads where reliable timing can be obtained, corresponding to the 13 vectors in Figure 3f. The ramp times of the dipolarization at the 6 spacecraft are marked by the boxes in Figure 3 panels c and d and listed in Figure 2. Note that although we place no restriction on the size of a triad, the typical separation among spacecraft in a triad is larger than 1 Re. Our dataset is dominated by triangles with large spacecraft separations. This is when the ramp times are well separated and thus

clearly resolved. For this reason, although TH-A/D/E routinely form local triangles, these triangles do not contribute much to the dataset because they often do not pass the timing criteria.

The velocity vectors show that the dipolarization propagation is everywhere azimuthal for this event. Because the propagation was azimuthal, we can quantify the azimuthal speed by fitting the ramp times and the corresponding MLTs to calculate the angular speed. Figure 3c shows that the angular speed is -2.1 deg/min, where negative value means eastward. We note that each velocity vector in Figure 3f is calculated from the corresponding triad (e.g. the triad of G15/THD/THE). The magnitude of a velocity vector is thus significantly averaged over the triad. For this reason, the azimuthal motion is more accurately determined by the linear fit. In Figure 3c, a linear fit is performed for the observed times of the dipolarization at each spacecraft and the corresponding MLTs. The r^2 of the linear fit is 1, suggesting that the azimuthal propagation was close to a pure rotation. The angular speed scales to ~ 25 km/s at 6.6 Re, which is comparable to the typical azimuthal phase speed of 30-50 km/s measured from 2-spacecraft timing (Nagai, 1982; Ohtani et al., 2018).

To estimate the azimuthal width of the dipolarization, which refers to the region of increasing tilt angle, we define the angular width $W = |\omega_{2D}| \min(\Delta T_i)$, where ΔT_i is the duration of the individual dipolarization at the satellites. In this event, $W = 10$ deg, which converts to an azimuthal width $W' = W \cdot 10 \text{ Re} \sim 1.8 \text{ Re}$ at the distance of 10 Re. W' is comparable to the typical value of 2 Re in previous studies (Liu et al., 2013; Huang et al., 2015). In addition, the spatial distribution of the spacecraft provides the lower limit of the radial and local time extent. Given that the propagation is determined as azimuthal, the local time extent (6 hr) is the minimum extent of the propagation whereas the radial extent (7 Re) is the minimum length of the structure. Based on these observations, the observed dipolarization was a finger-shaped structure, about 1.8 Re wide and at least 7 Re long (light blue region in Figure 3f), which propagated azimuthally from the local midnight to at least dawn (the blue arrow in Figure 3f). Figure 3d shows that misleading results can be obtained when only radial cuts of the data are examined. In this case, one would conclude that the dipolarization was first observed around 7 Re and propagated inward and outward. However, examination in both the azimuthal and radial directions shows that this is not the case for the August 28, 2014 event.

Figure 4 shows a similar event on January 09, 2008 in the post-midnight sector during a minor substorm at 11:40 UT (panel a). The propagation vectors can be determined at 3 triads (panel d) and again show an azimuthal propagation. A linear fit shows that the azimuthal propagation is close to a pure rotation (high $r^2 = 0.92$), with an angular speed of -1.6 deg/min (from linear fit, panel b). This value is consistent with $\omega_{2D} = -1.9 \pm 0.1$ deg/min, which is averaged from the velocity vectors. The angular width of the dipolarization was $W = 10$ deg, which scales to $W' = 1.8 \text{ Re}$ at 10 Re. The dipolarization was seen over 10 Re (10-20 Re, panel d), 2 hours in MLT (panel b), and 15 minutes in real time. Due to limitations related to available satellites and their orbits, a given event covers either a large radial distance but limited local time or a limited radial distance but large local time. The January 09, 2008 event is an example of the former whereas the August 28, 2014 event is the latter.

Two additional events in the pre-midnight sector are shown in Figure 5 and 6. Both events were associated with substorms of $AE > 500$ nT. In the March 28, 2017 event (Figure 5), an individual dipolarization was seen by 5 spacecraft during 15 minutes in real time. It propagated westward at an angular speed of 4.4 deg/min (linear fit, Figure 5b). The angular width was 8 deg, which scales to $W' = 1.4 \text{ Re}$ at 10 Re. The propagation was seen at least over 6 Re (6 to 12 Re) and 5 hours in MLT (-2 to -7 MLT, Figure 5b). In the February 29, 2008 event (Figure 6), an individual dipolarization was seen to propagate westward at 9.1 deg/min (linear fit,

Figure 6b). The propagation was at least over 10 Re (7 to 17 Re) and 4 hours in MLT (0 to -4 MLT). The angular width of this dipolarization (47 deg) is much larger than the previous dipolarizations. The statistical survey discussed in Section 4 shows that the angular width is typically 10 deg but can be much larger as in the February 29, 2008 event.

In the examples in Figures 3 to 6, the dipolarizations propagated azimuthally away from midnight, consistent with previous studies within geosynchronous orbit (Nagai, 1982; Ohtani et al., 2018). However, there are “unusual” dipolarizations that propagate azimuthally toward midnight most often in the pre-midnight sector. Figure 7 shows such an example on March 20, 2008. In this event, the angular speed was -3.5 deg/min (linear fit, Figure 7b). The angular width was 8 deg. The propagation was seen at least over 20 Re (8 to 28 Re) and 4 hours in MLT (-4 to 0 MLT). The reason for the “unusual” dipolarizations is unknown. A possible interpretation is that the center of the diverging propagation pattern sometimes shifts away from midnight. For example, the dipolarization shown in Figure 7 was first seen around -3 MLT. This is a possible location of substorm onset, which is likely to be the center of the divergence. Another possibility is that the unusual dipolarizations arise from some dayside processes (e.g., shock impact, dayside reconnection). For example, in Figure 15d, some eastward propagating dipolarizations are seen around -6 MLT, which is more likely to be related to dayside processes than substorm onset.

4 Statistical Properties

We initially identified 61 coherent dipolarization events, as described in Appendix C. Of those, 40 were azimuthally propagating, 66% eastward and 34% westward. The other 21 were radially propagating. As shown in Figure 15d, the eastward events (blue) are more often in the pre-midnight sector whereas the westward events (green) are mostly in the post-midnight sector. The distribution of the azimuthal events shows a diverging pattern where the separator is around [-3,0] MLT. Interestingly, this coincides with the typical MLT of auroral substorm onset (e.g. Liou et al., 2002). As discussed in Appendix C.5, there were also 21 events that propagated radially. Due to potential errors in determining the radial velocity (Section 2), we focus on the azimuthal events.

Using the same methods as in Section 3, we focus on the properties of the APDs including the propagation velocity v_{2D} , the angular speed ω , and the azimuthal width W' . These quantities can be directly determined from the 3-spacecraft timing measurements. In addition, quantities including the life time τ , which corresponds to when the dipolarization is first and last seen by the involved spacecraft, and the propagation extent in MLT and radial extent are also examined. Limited by the spacecraft distribution, these quantities only provide the lower limit of the real temporal or spatial extent. Figure 8 shows the histograms of the properties for the 40 ADPs. The azimuthal speed $|v_{2D}|$ (panel d) is ~ 50 km/s and the angular speed $|\omega|$ (panel e) is ~ 3 deg/min. These values are consistent with previous studies within and around geosynchronous orbit (Nagai, 1982; Ohtani et al., 2018). The azimuthal width W' (panel f) is on the order of 3-4 Re, but can be >10 Re in cases like the February 29, 2008 event (Figure 6). Panel a shows that the mean life time is at least 17 minutes. Panels b and c show that the average radial extent is 7.6 Re and the average propagation extent is 3.3 hr in MLT. In panel c, there are two peaks: one peak is around 5 Re, which corresponds to the dataset covering 4-12 Re, and a second smaller peak around 20 Re, which corresponds to the smaller THEMIS dataset covering 10-30 Re. The fact that the peaks are around the radial extent of both data sets suggests that the radial extent is likely to be much larger than the average value of 7.6 Re. In addition, as mentioned in Section 2, the radial extent would be larger due to the z-separation around the equatorial plane (Apatenkov et al., 2007).

Figure 9 shows the shape of all azimuthal dipolarizations in the equatorial plane. The region refers to the ramps of increasing tilt angle. The azimuthal width in Figure 8f and the radial extent in Figure 8b are used. To draw the boxes, we use the angular width determined through 3-spacecraft timing and assume it is the same over the full radial extent. Figure 9 shows that the azimuthal dipolarizations are typically finger-like, but can be wide sometimes (e.g., the February 29, 2008 event, Figure 6). The histogram insert shows the ratio of length over width. The average ratio is 2.8 and the ratio is greater than 1 for most events.

5 Discussion and Conclusion

The propagation of dipolarizations in the magnetotail has been previously statistically studied inside geosynchronous orbit (6.6 Re) and studies found slow (~ 50 km/s) azimuthal phase speeds (Nagai, 1982; Ohtani et al., 2018). In addition, other dipolarization related structures are known to propagate. Dipolarizing flux bundles (DFBs) have a fast (500 km/s) earthward phase velocity (Runov et al., 2009, 2011; Liu et al., 2013, 2014). Magnetic field pileups have a slow tailward and azimuthal expansion (Baumjohann et al., 1999; Nakamura et al., 2011). The APDs in our study have a typical angular speed of 3 deg/min, which scales to 30-50 km/s at 6.6 Re. This value is consistent with the dipolarizations studied by Nagai (1982) and Ohtani et al. (2018). Other similarities include the duration of the ramp of increasing tilt angle (5-10 min) and the divergent pattern around midnight. Therefore, we argue that the dipolarizations previously observed around geosynchronous orbit are the earthward portion of the APDs in our study. However, as we showed in Figure 9, the APDs can extend well beyond geosynchronous orbit, often penetrating into the mid-tail (20-30 Re).

We propose a possible picture for dipolarization propagation in the magnetotail, connecting the APDs reported herein to previously studied dipolarization structures (c.f. Figure 10). DFBs have life times on the order of several minutes, which is the time for earthward propagation at 500 km/s from 20 to 5 Re. After the first several minutes, all the trailing magnetic flux tubes form a slice of dipolarized region around a certain local time, corresponding to a finger-like cross-section in the equatorial plane. Two APDs expand both eastward and westward, in the next 20-30 min. This is the time for them to propagate from around midnight to local dawn and dusk at 3 deg/min. Both DFB and APD contribute to the tailward and azimuthal transport of magnetic flux, i.e., the expansion of the pileup region (Angelopoulos et al., 1996).

We note that the event criteria do not allow us to perform a robust study of how dipolarization structures propagate around midnight. This is due to two reasons. First, the 3-spacecraft timing technique requires a non-collinear geometry to robustly determine the propagation velocity. However, since the THEMIS spacecraft are designed to line up around midnight, we have a low count of possible events around midnight. This can be seen in Figure 16 and is explained in Appendix C. Second, timing along the earth-sun line shows that dipolarization structures around midnight propagate primarily radially: DFBs earthward and pileups tailward. As mentioned in Section 2, the z-separation of the spacecraft around the equator introduces significant error in determining the radial propagation velocities. Therefore, we cannot directly verify the tailward or earthward propagation for dipolarization structures around midnight. However, a possible synthesis picture is described above and in Figure 10.

Despite these limitations, our analysis approach is well suited to study azimuthally propagating dipolarizations. Based on the determined propagation velocity, we determined the azimuthal width to be 2.3 Re on average and ranges typically from 0.5 to 5 Re (Figure 8f). The value and range are consistent with previous studies of direct (Liu et al., 2013; Huang et al., 2015; Nakamura et al., 2002) or indirect (Ohtani et

al., 2018) measurements. In addition, we show that the APDs are radially extensive (7.8 Re on average, Figure 8c). This raises questions about how the magnetotail couples to the auroral ionosphere. Dipolarizations around geosynchronous orbit are often discussed in the context of current systems related to substorms (McPherron et al., 1973; Kepko et al., 2015, and references therein). It is thought that the region II current couples the nightside auroral ionosphere to the near-earth tail. However, if these dipolarizations are the earthward portion of ADPs, then they extend well into the mid-tail, how such radially extensive dipolarizations are coupled to the ionosphere needs further investigations.

Based on the azimuthal width and radial extent, we show that the azimuthally propagating dipolarizations are often finger-like structures (Figure 9). The structure refers to the region of increasing tilt angle, which is usually associated with high magnetic gradients. Such structures provide a possible mechanism for transporting energetic particles through gradient B drift, which is suggested in simulations (e.g. Ukhorskiy et al., 2018; Gabrielse et al., 2017). In the August 28, 2014 event in Figure 3, the gradient associated with the dipolarization $\nabla|B|$ ranges from 50 to 200 nT/Re. This gradient is much larger than the gradient of 1 to 10 nT/Re associated with the background magnetic field. The large gradient, presumably aligns with the 2D shape of the dipolarization, provides an elongated radial channel for keV to MeV particles to transport inward or outward. Furthermore, the APDs are enduring (last several 10s minutes) and can propagate well into the dayside. Sergeev et al. (2006) report evidence for a diverging propagation of flapping motions in the magnetotail (10-30 Re). Although flapping events are explicitly excluded in our dataset (Section C), the APDs have similar radial extent and propagation pattern as the flapping motion of the plasma sheet. The similarities raise questions on the physical relation between the two phenomena.

In summary, the propagation of dipolarizations in the Earth's magnetotail was studied using 3-spacecraft timing. We provide observational evidence for a class of dipolarizations that propagate azimuthally at the angular speed of ~ 3 deg/min, which scales to ~ 50 km/s at 6.6 Re. These structures are often finger-like in shape, several Re wide and 5-20 Re long. The structures sweep across the magnetotail during the course of 20-30 min and often reach out well into the dayside. These observations raise questions related to several fundamental processes during geomagnetic storms/substorms, including the possible connection to other dipolarization structures (dipolarizing flux bundle and pileup), the azimuthally propagating flapping motion of the plasma sheet, a possible mechanism for efficient radial transport of keV to MeV particles through gradient B drift, and the coupling to the auroral ionosphere.

Acknowledgments

The authors thank the following teams for providing the magnetic field data, including RBSP/EMFISIS, GOES magnetometer, MMS/FGM, and THEMIS/FGM. This work was supported at UMN by the NASA grant 80NSSC19K0306 and by the contract from JHU/APL under NASA prime contract NAS5-01072. The magnetic field data used in this work are all available online. The RBSP data are at <https://cdaweb.gsfc.nasa.gov/pub/data/rbsp>. The THEMIS data are at <http://themis.ssl.berkeley.edu/data/themis>. The GOES data are at <https://satdat.ngdc.noaa.gov/sem/goes/data>. The MMS data are at <https://cdaweb.gsfc.nasa.gov/pub/data/mms>.

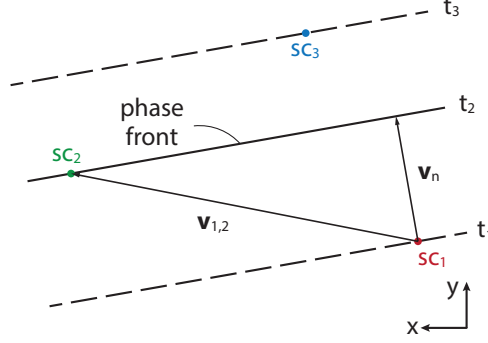


Figure 1. Measuring the 2D propagation speed \vec{v}_n of a dipolarization in the x-y plane using 3 non-collinear spacecraft. Note that the phase velocity $|\vec{v}_{1,2}|$ measured by a 2-spacecraft timing is in general larger than $|\vec{v}_n|$, especially when the spacecraft separation is perpendicular to $\vec{v}_{1,2}$.

Appendix A Method used to detrend tilt angles and identify dipolarizations

By definition, dipolarizations correspond to a sudden increase of the poloidal tilt of the magnetic field. Therefore, dipolarization identification involves the detection of the region over which the tilt angle increases, which we call the “ramp”. The change of tilt angle, which is the key information, needs to be extracted from the background magnetic field change, which decreases more than one order magnitude from within 6.6 Re to 10-30 Re. Thus, to enable inter-comparison at all distances, the tilt angle of the measured magnetic field $B_{x,y,z}$, defined as $\alpha_{\text{meas}} = \arcsin(B_z/|B|)$ in the SM coordinate, is detrended as follow. A slowly varying background due to the spacecraft motion within the earth’s dipole field is estimated by the T89 model (Tsyganenko, 1989) with default inputs, from which the associated model tilt angle α_{T89} is calculated. The difference, $\alpha_{\text{meas}} - \alpha_{\text{T89}}$, is then detrended through a 60-min boxcar average to remove residue offsets. Figure 11 illustrates the background removal using an example at THD in the August 28, 2014 event. Panel a shows the original tilt angle α_{meas} (black) and panel b shows the detrended tilt angle θ (black). The background ($= \theta - \alpha_{\text{meas}}$) is shown as the blue curve in panel a. It is clear that the detrended tilt angle θ retains the large scale fluctuations in the original tilt angle data.

Detection of ramps with the appropriate change in tilt angle is performed by an automated algorithm based on the detrended tilt angle θ . Because the detrended tilt angle θ fluctuates around 0 due to the boxcar averaging, a ramp is identified as a region of positive slope about 0. As shown in Figure 11c, the start and end times (t_S and t_E) of the ramp are defined as where $d\theta/dt$ exceeds its local standard deviation by 1 sigma. Consequently, the algorithm further determines (1) the duration $\Delta T = t_E - t_S$, (2) the change of tilt angle $\Delta\theta = \theta(t_E) - \theta(t_S)$, and (3) the “ramp time” $= (t_E + t_S)/2$. To remove small scale fluctuations on top of the main ramp, θ is smoothed over a 2-min window (non-smoothed θ are used in all other calculations). The smoothed version is shown in Figure 11b (red).

A initial survey of the detected ramps showed that a small fraction of them were flapping events, boundary crossings, and ULF waves. These ramps are either quasi-periodic, or contain abrupt (< 1 min) and large (> 80 deg) changes in $\Delta\theta$. To exclude

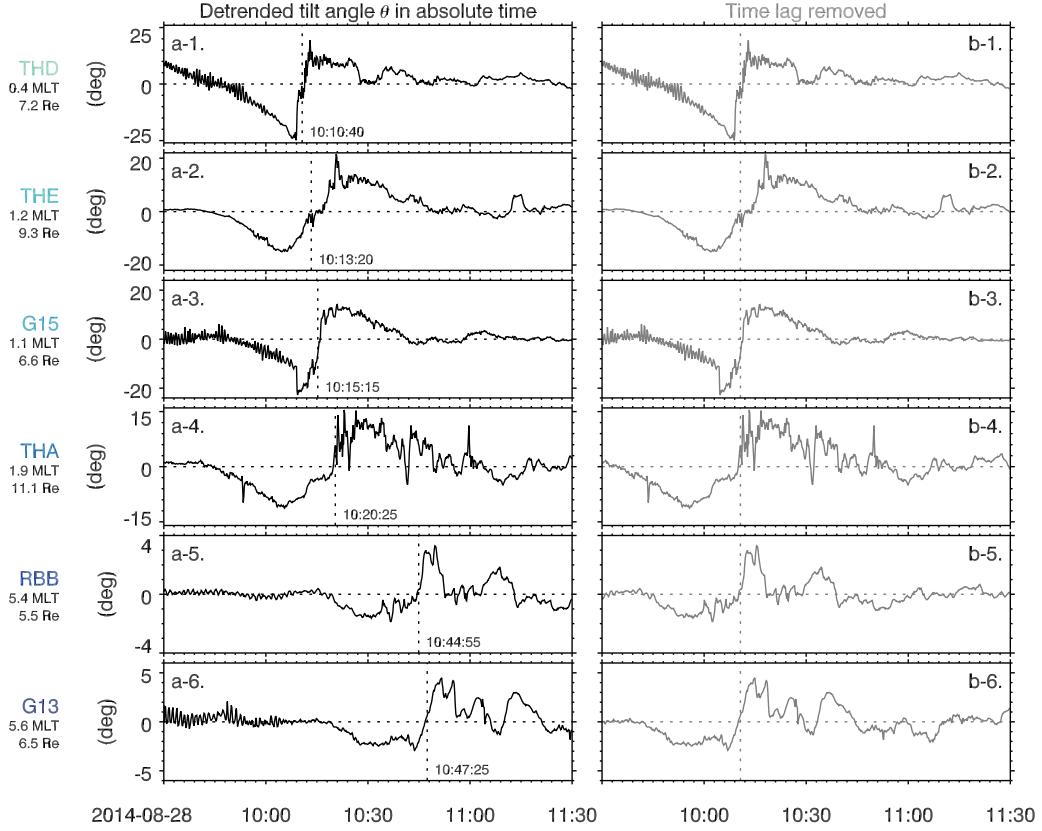


Figure 2. The detrended tilt angle θ in real time (left) and after removing the time lags (right), during the August 28, 2014 event. An individual dipolarization was observed at 6 satellites during the course of ~ 30 min. The duration of the ramp of increasing tilt angle ranged about 5-10 min at the satellites. The vertical dashed line in the left panels indicates the "ramp time" of the dipolarization at each satellite. Data in the right hand panels are aligned according to the ramp time. Details on detecting ramps and dipolarizations and detrending the tilt angle are explained in Appendix A.

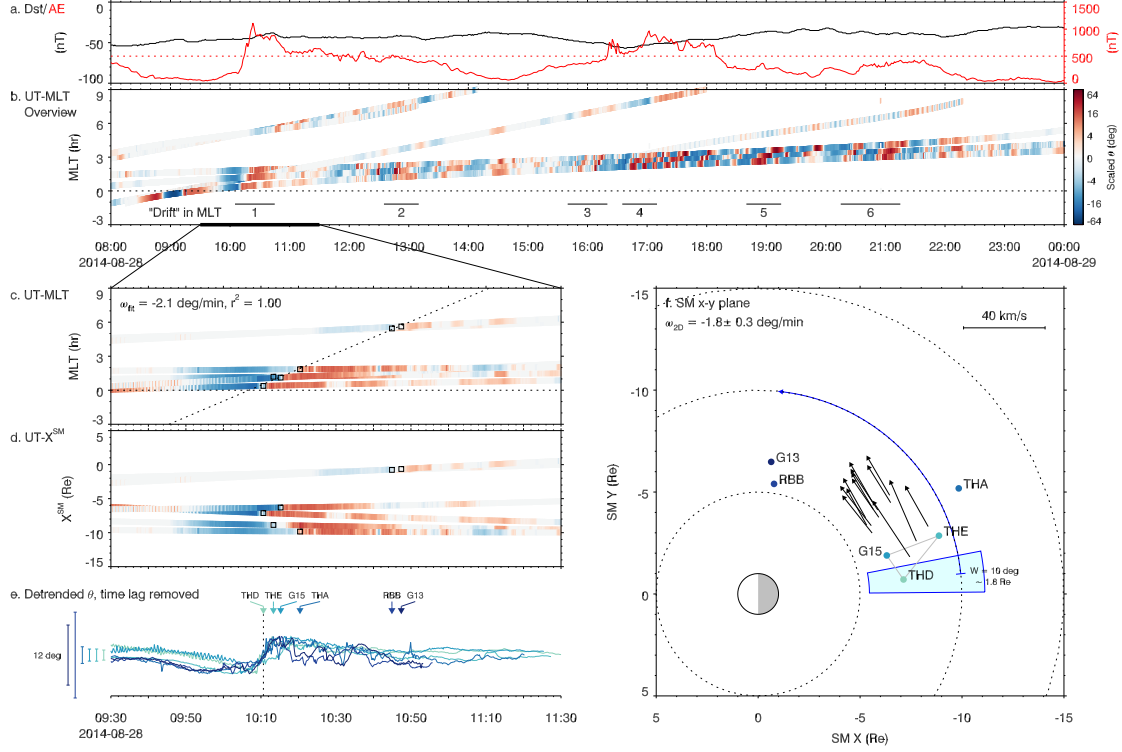


Figure 3. The dipolarization signatures during the recovery phase of a storm on August 28 2014. Panel a shows the Dst and AE indices. Panel b shows the detrended tilt angle color-coded along spacecraft trajectories in the UT-MLT plane. θ is scaled by $\exp(-z^2/2)$, where $z = \text{MLT}/4$, to compensate the decay of θ in MLT (c.f. Figure 12). Panel c zooms in to a section of panel b. Panel d shows the same data on the UT-X plane. Panel e shows with time lag removed (same data in Figure 2). The arrows indicate the ramp times in real time and bars on the left shows the y-scale. Panel f shows the velocity vectors of propagation at all triads. A triad is when a triangle is sufficiently non-collinear and 3-spacecraft timing can be robustly done. The foot of each arrow is at the center of the corresponding triad (e.g., the triad among G15/THD/THE). The inferred 2D shape of the dipolarization and its propagation extent are marked by the blue region and the curved arrow. As shown in panel f, the propagation was primarily azimuthal. Given that the propagation is, a linear fit is done for the ramp times and MLTs (panel c, dotted line) to quantify the angular speed. The high r^2 of the linear fit suggests that the propagation is close to a pure rotation. Note that the vectors in panel f are not local velocities but averaged over the corresponding triad. For this reason, their magnitudes are all comparable. In principle, local speed should scale with distance for a pure rotation.

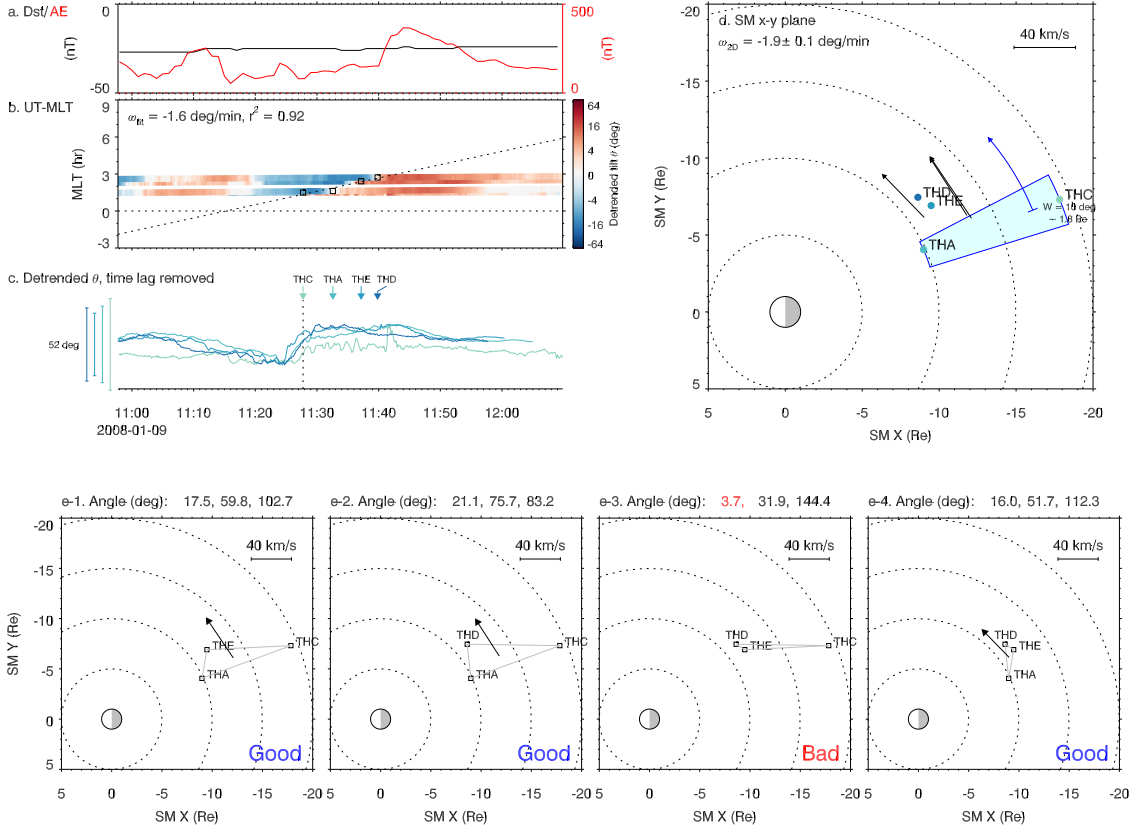


Figure 4. The dipolarization signatures and timing results for the January 09, 2008 event. Panel a-d are in the same format as panel a, c, e, f in Figure 3. Panel e-1 to e-4 show all 4 tri-angle combinations out of the 4 available spacecraft. 3-spacecraft timing is performed in the 3 triads of good geometry. This example shows another dipolarization in the post-midnight sector, which extended from 10 to 20 Re.

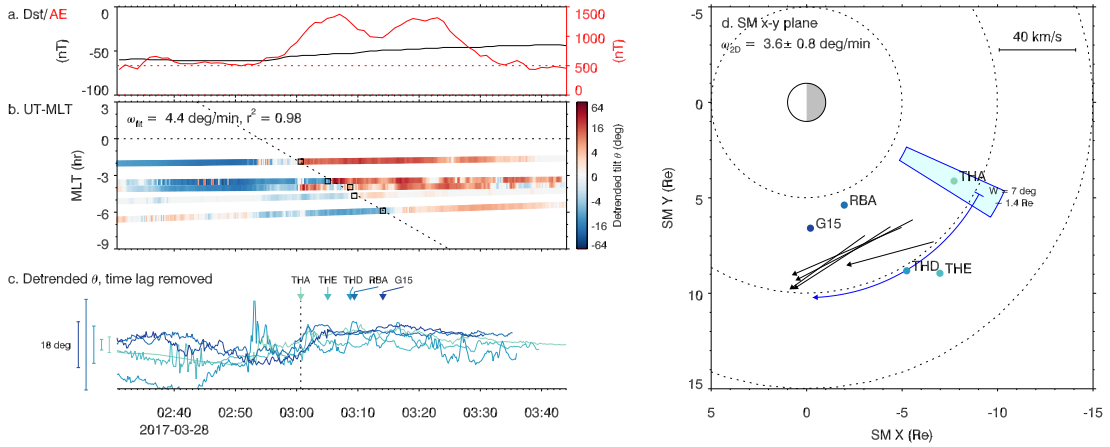


Figure 5. The dipolarization signatures and timing results for the March 28, 2017 event. Panels are in the same format in Figure 4. This examples shows a dipolarization in the pre-midnight sector.

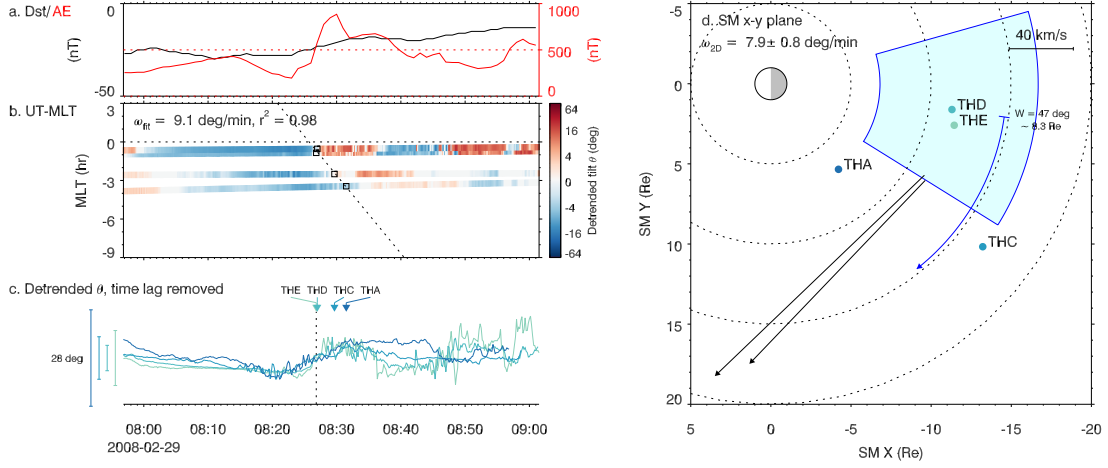


Figure 6. The dipolarization signatures and timing results for the February 29, 2008 event. Panels are in the same format in Figure 4. This example shows a dipolarization which was very wide in azimuth.

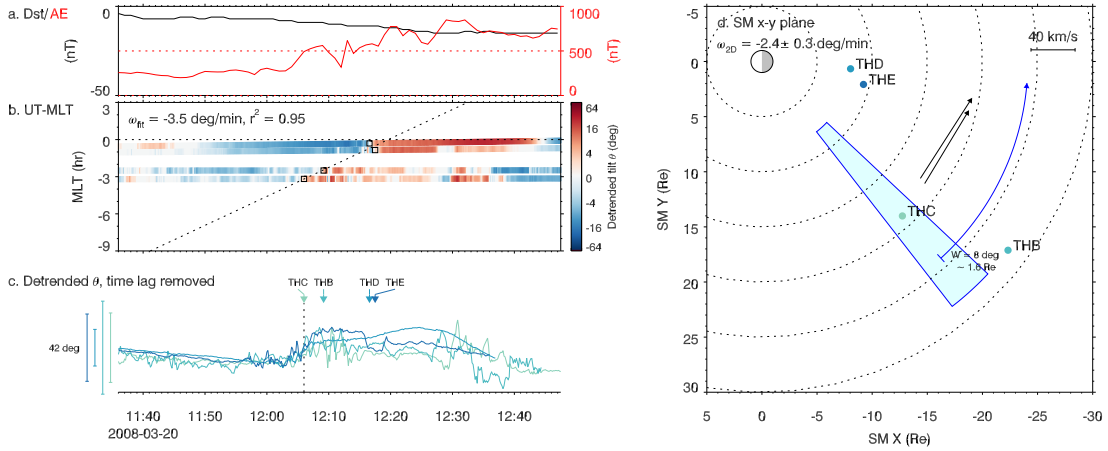


Figure 7. The dipolarization signatures and timing results for the March 20, 2008 event. Panels are in the same format in Figure 4. This example shows a dipolarization propagated azimuthally toward the midnight.

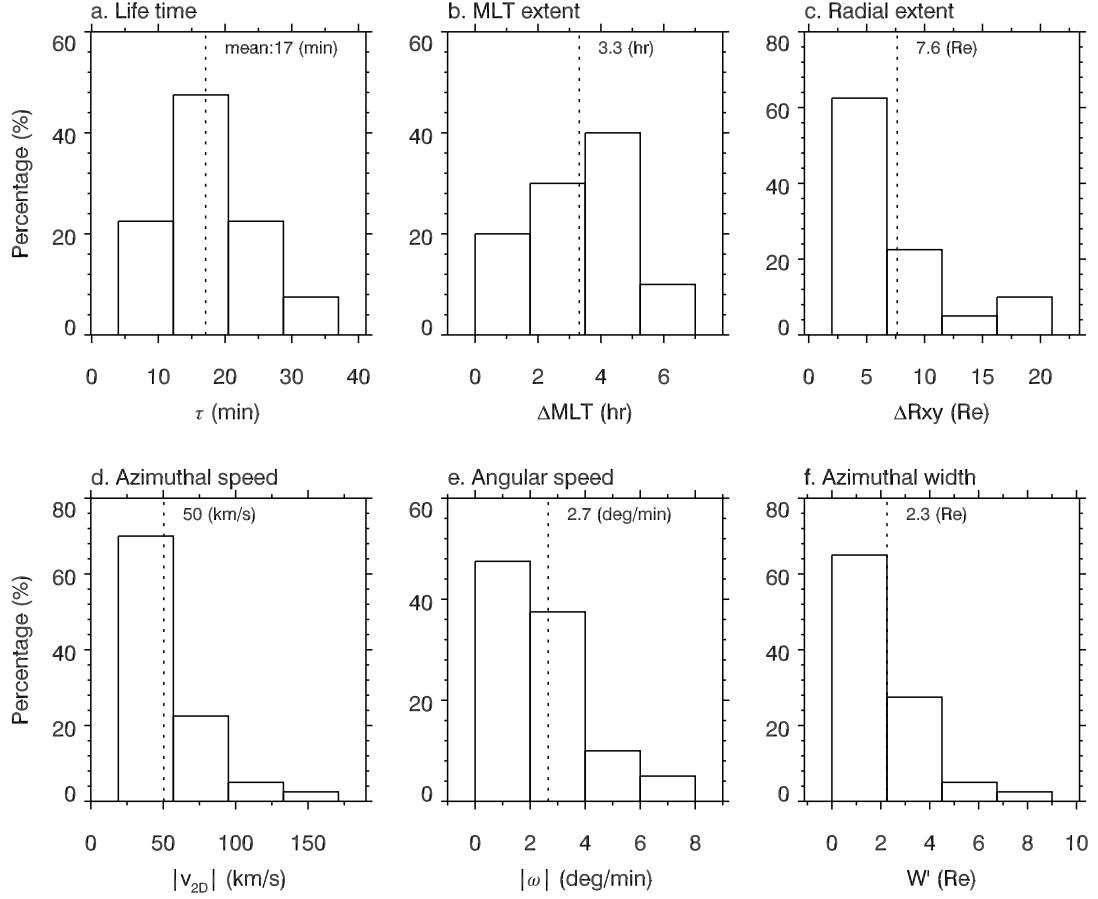


Figure 8. Properties of the azimuthal dipolarizations. In each panel, the histogram shows the distribution of the property and the mean value is marked by the vertical line.

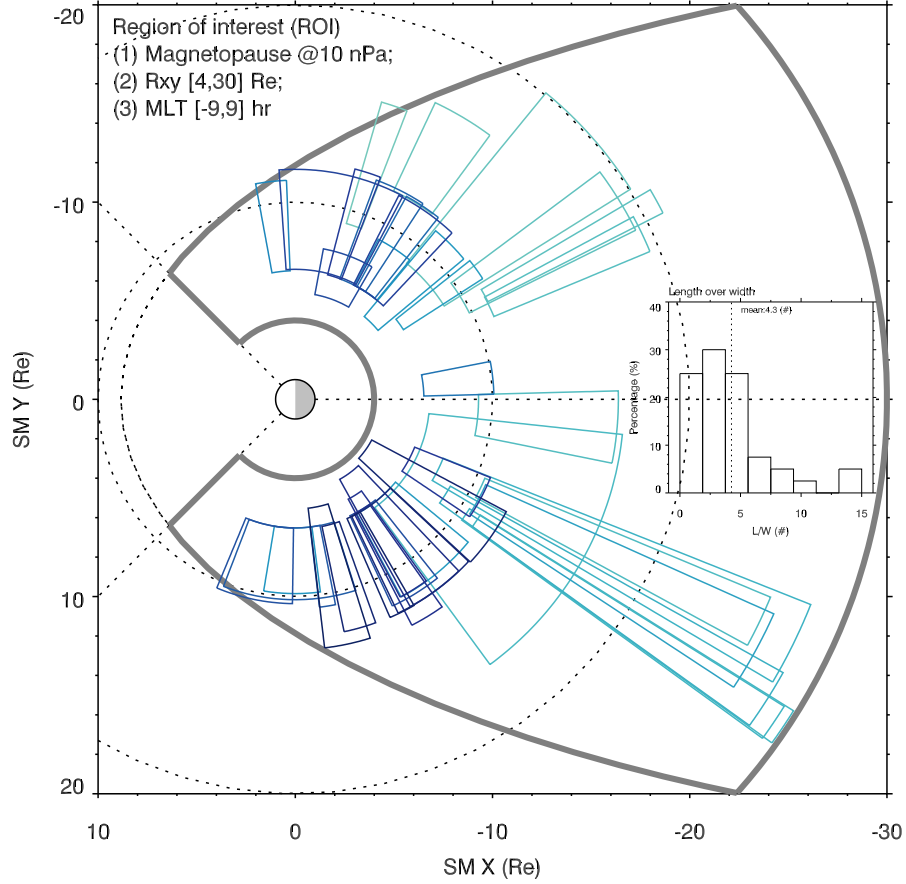


Figure 9. The 2D shape of all azimuthal dipolarization events. The events are differentiated by color, to help resolve overlapping shapes. For each event, the 2D shape is determined by the radial extent of the involved spacecraft and the angular width W . The center of the 2D shape is at the center of the MLT of the propagation extent. The figure and the histogram show that the structures are often finger-like and radially extensive. Note that the darker events often range from 5-12 Re, which is probably limited by spacecraft distribution.

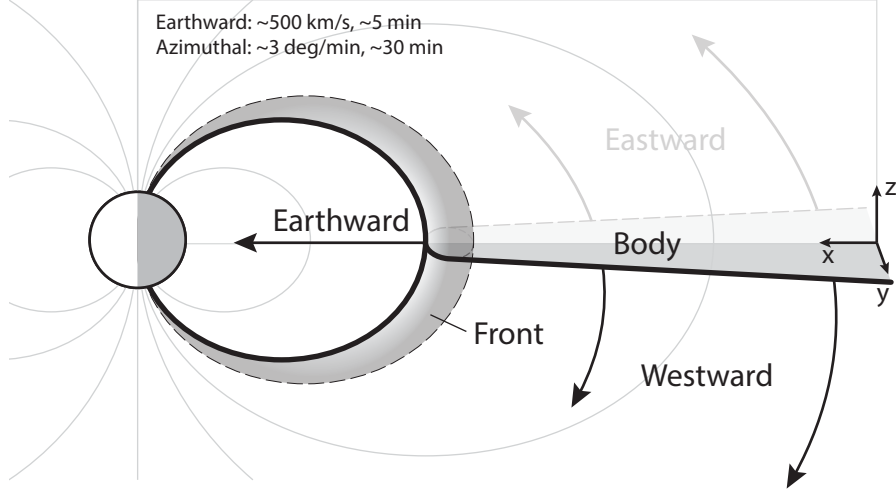


Figure 10. A model to illustrate the azimuthal expansion of the dipolarization structures reported in this study. The azimuthal expansion is likely to be closely related to dipolarizing flux bundles, which have been extensively studied.

them, we select ramps that are isolated and with a clear step-up increase of tilt angle. The criteria are: (1) the duration of the ramp $\Delta T > 1$ min; (2) the change of tilt angle $\Delta\theta < 80$ deg; (3) the next ramp detected by the same spacecraft is after > 10 min; and (4) the tilt angle θ remains positive > 8 min in total or > 4 min continuously in the same 10 min. In addition, to focus on the largest events, we select the ramps with $\Delta\theta \cdot e^{(MLT/4)^2/2} > 8$ deg. The scaling factor arises to compensate the decaying trend of $\Delta\theta$ in MLT. In Figure 12, $\Delta\theta$ of 40,000 randomly selected ramps (before the above criteria are applied) are binned every 2 hours in MLT. Percentile contours at 10%, 50%, and 90% levels of the sorted data over the bins show a decay in MLT. The contours are empirically modeled by $e^{-z^2/2}$, resulting in a decay rate of $z \sim MLT/4$. Based on the percentiles, the criteria $\Delta\theta \cdot e^{(MLT/4)^2/2} > 8$ deg selects the top 25% ramps. In summary, ramps pass all above criteria are isolated dipolarizations with significant jump in tilt angle and remain dipole-like after the jump.

Appendix B Cross-correlation analysis on dipolarizations

Cross-correlation analysis is used to determine the coherency of dipolarizations seen on 2 satellites and to limit the errors in the 3-spacecraft timing. The identification algorithm described in Appendix A not only identifies a dipolarization but also determines its duration ΔT , which is the width of the ramp of increasing tilt angle, and its ramp time, which is the center time of the ramp. The window size for the cross-correlation is chosen to be 5 times the smallest of the ΔT of the 2 dipolarizations. The cross-correlation is calculated over this window size centered around the ramp time for each satellite. Figure 13 shows the cross-correlation results for the dipolarizations in the August 28, 2014 event. To follow the temporal evolution, the 6 dipolarizations are sorted by their ramp times, forming 5 pairs for cross-correlation. In panels on the right, the error associated with the cross-correlation is calculated according to Equation (1.7) in Paschmann and W. Daly (2008)

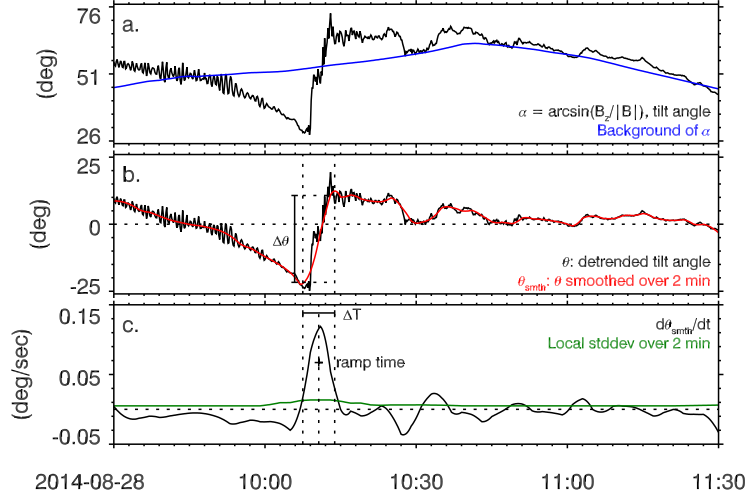


Figure 11. An example showing the algorithm to detect a ramp of increasing tilt angle and determine its properties. Panel a shows the tilt angle α calculated from the measured magnetic field in solar magnetic (SM) coordinates. The T89 model of the earth’s magnetic field is subtracted and the result is detrended using a boxcar average over 60 min. Panel b shows the detrended tilt angle θ . A dipolarization corresponds to a positive slope centered around 0. To focus on the main ramp associated with a dipolarization, the tilt angle is smoothed over 2 min to remove small scale fluctuations. Panel c shows the derivative of the smoothed θ (black) and its local standard deviation over 2 min (green). The start and end times (t_S and t_E) of the ramp are identified as where $d\theta/dt$ exceeds the local standard deviation by one sigma. Consequently, we define the duration $\Delta T = t_E - t_S$, the change of tilt angle $\Delta\theta = \theta(t_E) - \theta(t_S)$, and the “ramp time” = $(t_E + t_S)/2$ for the ramp. In Appendix A, we further identify isolated ramps which correspond to dipolarizations, as quasi-periodical ramps correspond to flapping event, boundary crossings, and ULF waves.

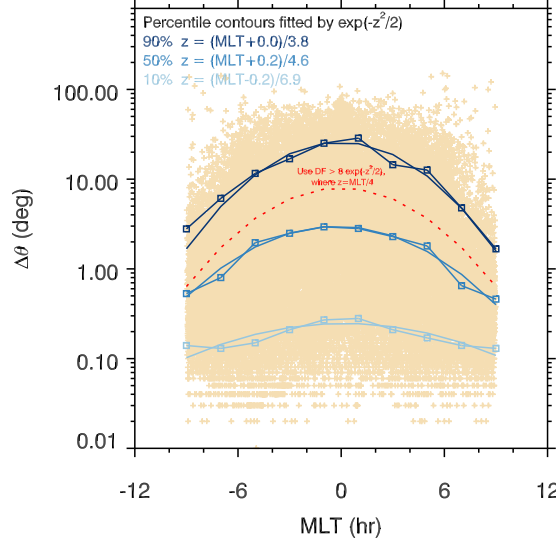


Figure 12. Change of tilt angle $\Delta\theta$ versus MLT for 40,000 randomly selected ramps identified in the region of interest. The $\Delta\theta$ data are binned every 2 hours in MLT and sorted within each bin. Percentile contours at 10%, 50%, and 90% levels of the sorted data over the bins are plotted and empirically fitted by $e^{-z^2/2}$, resulting in a decay rate of $z \sim MLT/4$. To select the top 25% ramps, we use the criteria $\Delta\theta \cdot e^{(MLT/4)^2/2} > 8$ deg.

$$(\text{err})^2 = \frac{1}{M-1} \frac{1-cc}{cc} \frac{2\langle\delta\theta^2\rangle}{\langle(d\theta/dt)^2\rangle},$$

where M is the number of data points, cc is the maximum cross correlation, $\langle\delta\theta^2\rangle$ is the average square of the deviation of from its mean value, and $\langle(d\theta/dt)^2\rangle$ is the average slope square of θ . Because the calculated uncertainty is typically much smaller than the data rate (10 sec), it is not used in the error analysis. Instead, we require that the timing results based on the two methods, cross correlation and ramp time difference, must agree. For each triad, we require that the two methods to provide consistent velocity vectors: (1) the magnitude difference is $<20\%$; and (2) the angle difference is <30 deg. Because the criteria ensure that timing results are essentially the same from the two methods, for simplicity, we use the timing results based on the ramp times in the figures throughout this paper.

Appendix C Event Selection for Azimuthally Propagating Dipolarizations

The examples of dipolarization structures shown in Section 3 motivated a procedure to search for similar events. To robustly determine the propagation, the velocity vector is required to be consistently determined by at least two triads, involving a minimum of 4 spacecraft per event. The event selection procedure is summarized in Table 1, Figure 16, and described below.

C.1 Step 1: Identify dipolarizations in ROI

For each satellite, we search for dipolarizations with a steady (> 1 min) and well-defined step-up ramp of the tilt angle (see Appendix A for further details). To exclude

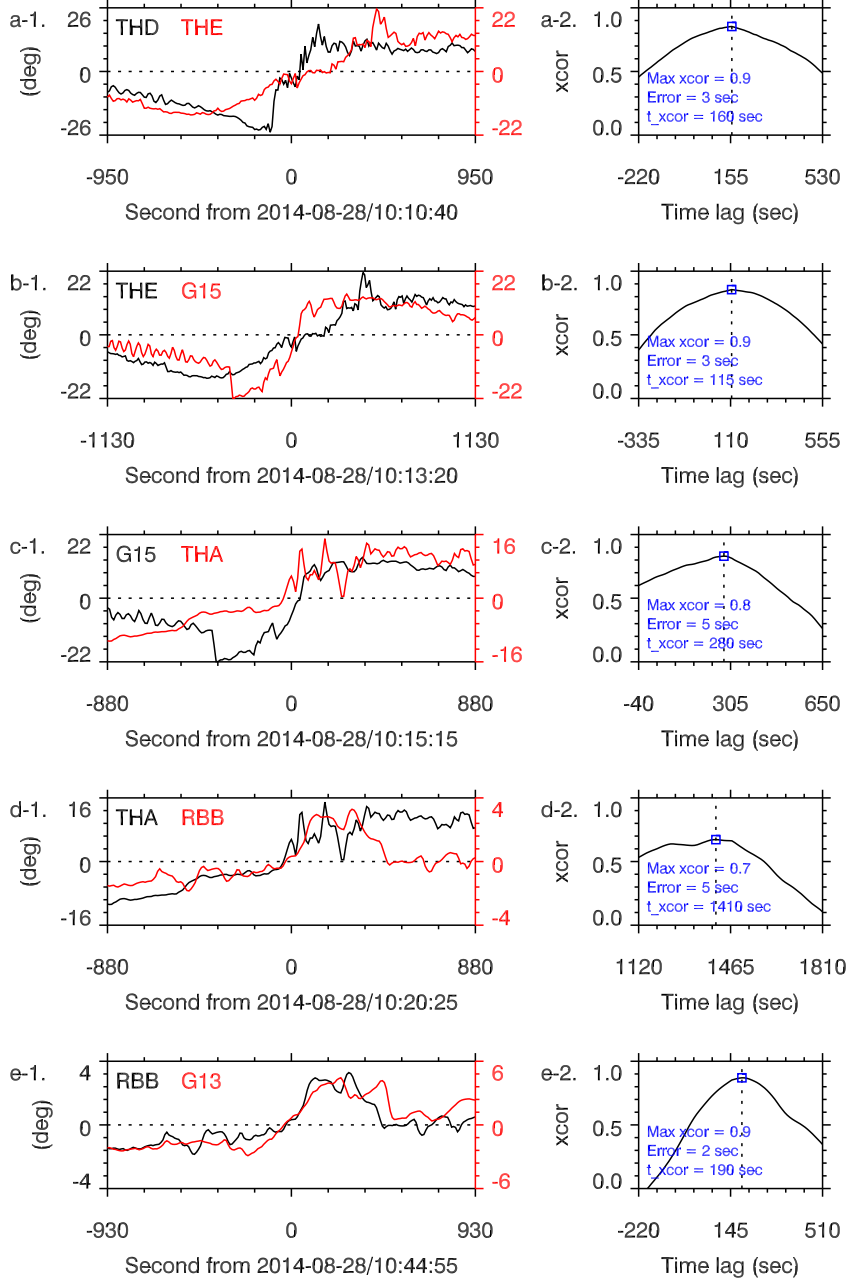


Figure 13. Cross-correlation between spacecraft pairs in the August 28, 2014 event. In each row, the left panel plots the data within the window of cross-correlation after the proper time lag removed in black (red) for the first (second) satellite. The window size is 5 times the smallest of the ΔT of the two dipolarizations. The right panel plots the cross-correlation as a function of time lag. The center of the x-axis is the difference between the ramp times of the two dipolarizations. The time lag corresponding to the maximum cross-correlation is marked by the vertical dashed line. The deviation from the center is the difference of time lags from the two methods: ramp time difference and cross correlation. The uncertainty of cross-correlation itself, calculated based on Equation (1.7) in Paschmann and W. Daly (2008), is listed in the right panels but not used for error analysis because it is much smaller than the data rate of 10 sec of the tilt angle θ .

Table 1. Event selection procedure for dipolarizations (DPs). The “rate” refers to the ratio of the number of dipolarization in the previous over the current step.

ID	# of DP	Rate	Description
1	19,584	N/A	All isolated DPs identified per involved spacecraft (SC).
2	1,909	10%	A subset of all, when an individual DP is seen by >3 SC, but also contains stochastic DPs which are transient or local.
3	737	38%	Coherent DP candidates, when an individual DP is seen by >3 SC and the propagation vectors are robustly determined. Stochastic DPs are removed through coherency analysis.
4	274	37%	Coherent DP events, when the propagation is along a certain direction.

ULF waves, flapping events, and boundary crossings, which include quasi-periodic increases in the tilt angle, isolated dipolarizations are selected, where the satellite sees no other dipolarization in 10 min. The search is within a “region of interest” (ROI, c.f., Figure 16) between 4 and 30 Re radial distance and within ± 9 MLT of midnight. In addition, the ROI was bounded using the Shue model of the magnetopause (Shue et al., 1998) with a high dynamic pressure (10 nPa) as the input, to exclude magnetopause crossings which may resemble dipolarizations. Two searches within the ROI are performed. The first was between 4 and 12 Re over 5 years (Oct 2012 to 2017) using RBSP-A/B, TH-A/D/E, GOES-13/14/15, and MMS-1. The second search extended from 12 to 30 Re, using 2.5 years of data from TH-A/B/C/D/E. In all, 19,584 dipolarizations on a single spacecraft level were identified (Figure 16a). As expected, most dipolarizations are identified around the apogee of the spacecraft, for example, around 10 Re for TH-A/D/E and around 20 Re for TH-C. Figure 14 shows all dipolarizations identified during 4 hours around the August 28, 2014 event. The figure also shows that although the identified dipolarizations are isolated, i.e., a given spacecraft sees only 1 dipolarization in the 10-minute window, each dipolarization as seen by different spacecraft could be either closely spaced in ramp time or very separated in ramp time.

C.2 Step 2: Apply a mathematical filter to scale down the search

Figure 14 shows the construction of a spacecraft sequence, which is used to select the dipolarizations which could provide robust 3-spacecraft timing (about 10% of all identified dipolarization). Dipolarizations are weaved together and sorted on the basis of the ramp time, resulting in a spacecraft sequence that includes a set of dipolarizations sorted on the basis of consistent spatial location and ramp time. The spacecraft sequence is critical for selecting events because it carries information on how the temporal evolution of a dipolarization can be observed by randomly distributed spacecraft. For example, a dipolarization which propagates in a certain direction can be systematically seen by many spacecraft en route. Such a situation corresponds to a section in the spacecraft sequence without a given spacecraft appearing more than once in the sequence (i.e., seeing what must be two different dipolarizations), for example, the section of the first 6 spacecraft (THD-THE-G15-THA-RBB-G13) in Figure 14. In this study, we select the sections to contain >3 different spacecraft so that the propagation direction and speed can be determined at at least two locations. The section (THD-THE-THA) at the end of the time interval is rejected because the section contains only 3 spacecraft. The figure also shows another type of dipolarization, which is stochastic in the sense that the dipolarization is local in space or time. For example,

the dipolarization around 12:30 UT is only seen by THA. The selected sections may contain such stochastic dipolarizations. We eliminate sections that contain stochastic dipolarizations through coherency analysis as explained in Section C.3. Here we emphasize that the spacecraft sequence is random, meaning not space/time ordered in a consistent propagation sense. Because the spacecraft have very different orbits, there is not always a consistent spacing in radial distance and local time. THA, THD and THE are always consistently spaced in MLT for this interval, while the geosynchronous spacecraft may see a given event at any MLT. Based on the randomness, the chance of finding a section with m different spacecraft when n spacecraft is available in a random sequence is P_n^m/n^m (P for permutation). The theoretical selection rate is $c(n) = \sum_{m=4}^n P_n^m/n^m$. In typical cases, the number of available spacecraft is $n = 4, 5, 6$, thus $c(4) = 9\%$, $c(5) = 23\%$, $c(6) = 33\%$. Figure 16b shows that the actual selection rate is larger as more spacecraft are available closer to earth. The actual selection rate tends to be smaller than the theoretical value because n could be smaller than 4. In Figure 16b, the selection rates are 0 in the green bins because the original counts are low (Figure 16a) and thus the expectation is ~ 0 . In all, 606 sections containing 1,909 dipolarizations are selected, which corresponds to an average selection rate of 10% (19,584 total).

C.3 Step 3: Select coherent dipolarization candidates

Within each selected section, stochastic dipolarizations are eliminated by requiring that (1) dipolarization pairs adjacent in ramp time are within 30 min; (2) the average time separation of all pairs < 8 min; and (3) the average cross-correlation of all pairs > 0.5 . The first two criteria ensures that a propagating dipolarization is sampled consistently and continuously in time, whereas the third criterion ensures the coherency. Note that although each dipolarization is isolated in the sense that no other dipolarization is seen by the same spacecraft within 10 min, two dipolarizations adjacent in ramp time and from different spacecraft can be close in time. Next, Equation (2) is solved based on both the time difference of the ramp times and on the time lags of maximum cross-correlation. As described in Section B, for each triad, the two methods must agree to within 20% for the velocity magnitude and within 30 deg for direction. For simplicity, we use the velocity vectors based on the ramp time difference in the paper. Using this approach, we identified 164 sections containing 737 dipolarizations on a single spacecraft level, which we call the “coherent dipolarization” candidates. These are events when similar dipolarization signatures are seen at > 3 spacecraft and the propagation vectors can be robustly determined in > 2 triads. The selection rate is 38%, (737 selected from 1,909 dipolarizations, Figure 16c), providing a crude estimation on the occurrence rate of what we defined to be a coherent dipolarization among general dipolarizations: for a certain isolated dipolarization observed by a satellite, there is a high chance (38%) that the dipolarization propagates coherently in space.

C.4 Step 4: Select coherent dipolarization events

Each of the 164 candidates contains at least two robustly determined propagation vectors. 61 of them, which we call the coherent dipolarization events, show propagation in a consistent direction, i.e., the scatter of the vectors is small. Specifically, the standard deviation of the direction is < 20 deg and the standard deviation of the magnitudes is $< 30\%$ of the mean. The other candidates, however, contain inconsistent velocity vectors, which could due to several reasons. For example, the propagation vectors are diverging if the region enclosed by the spacecraft is where an individual dipolarization develops. The propagation vectors could be inconsistent in direction for a dipolarization with a corrugated phase front. In the rest of the paper, we will focus on the 61 coherent dipolarization events, because they present the simple situation when

an individual dipolarization propagates along a certain direction within the region enclosed by the involved spacecraft.

C.5 Azimuthally propagating dipolarizations

We have identified 61 coherent dipolarization events as described in the previous sections. Of those, 66% (40 events) propagated primarily azimuthally (41% eastward and 25% westward), while the rest 34% (21 events) propagated radially (21% inward and 13% outward). Figure 15 shows the distribution of the events in MLT. In the figure, the azimuthal events are marked as the blue and green points and the radial events are marked by purple and red points. The distribution of the points follows the picture of cylindrical coordinate (radial-azimuthal, panels a and b), not the Cartesian coordinate (x-y, panel c).

We note that although the propagation velocities in the 61 coherent dipolarization events are robustly determined, the robustness, referring to the 3-spacecraft timing technique, can be affected by the z-separation around the magnetic equator. As mentioned in Section 2, the z-separation primarily affects the radial but not azimuthal propagation velocities. The z-separation may cause uncertainty in determining the radial distance of the spacecraft in the magnetic equator. The uncertainty introduces potential error in the radial speed, however, radial events are still radial because the radial separation of the spacecraft is typically larger than the uncertainty, i.e., the propagation direction is unlikely to be affected. Therefore it is interesting that the number of radial events is roughly 1/2 of the azimuthal events. This is consistent with the picture shown in Figure 15, where one radially propagating dipolarization is accompanied by two azimuthally propagating dipolarizations in eastward and westward. In addition, a significant number of these radial events are propagating tailward. The potential abundance of tailward propagating dipolarization has not been documented before. The tailward propagation may be related to physical processes like the pile-up of magnetic fluxes (Baumjohann et al., 1999) or near-earth reconnection (Angelopoulos et al., 2020).

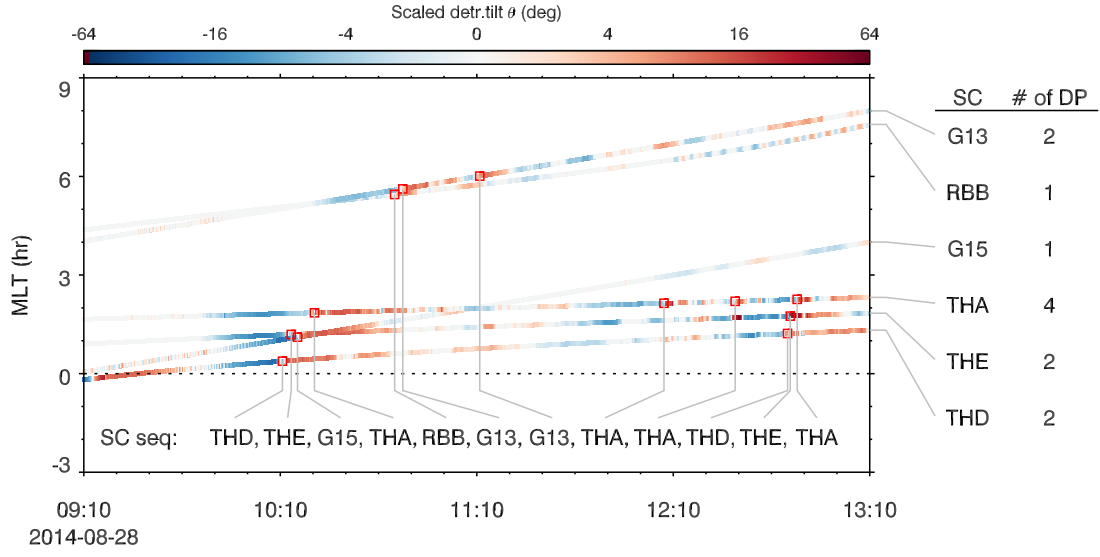


Figure 14. The location in MLT and UT of each dipolarization (red box) identified during this 4 hour interval around the August 28, 2014 event. The plot is in the same format as Figure 3b. For each spacecraft track, the corresponding spacecraft is explicitly marked, to illustrate how a spacecraft sequence is constructed from the dipolarizations identified on each spacecraft. The spacecraft sequence, obtained by sorting the dipolarizations using the ramp time for each spacecraft, is used to select the dipolarizations which could provide robust 3-spacecraft timing (Section C.2).

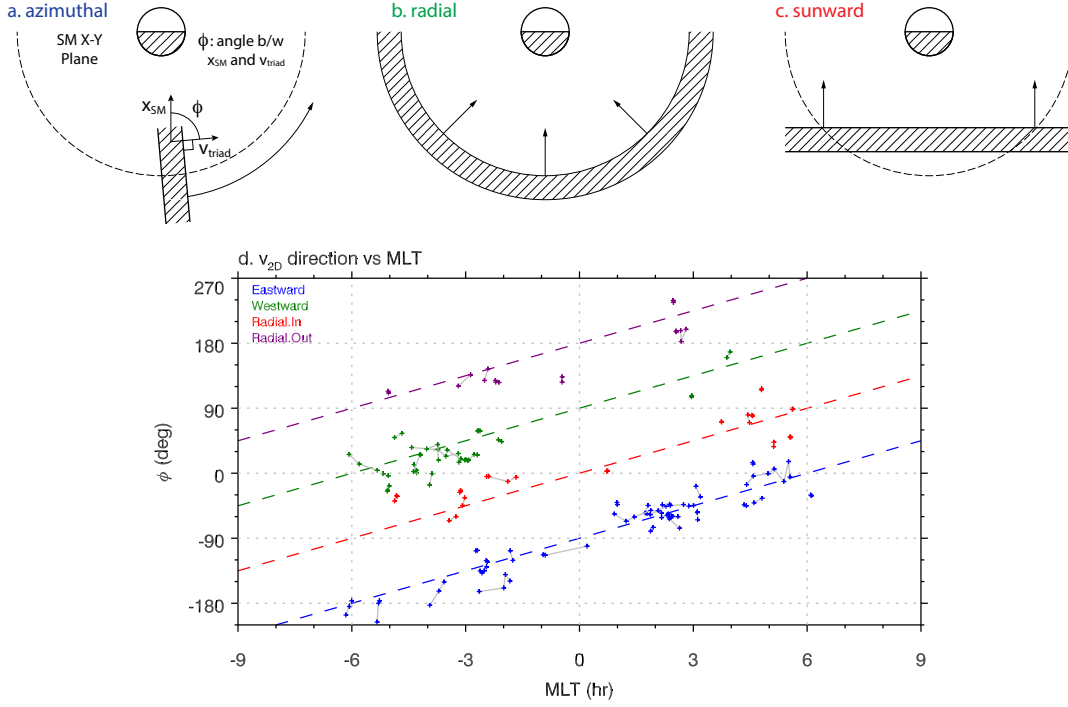


Figure 15. Direction of the velocity vectors \vec{v}_{2D} as a function of MLT for the coherent dipolarization events. Schematics of dipolarization propagate (a) azimuthally, (b) radially, and (c) sunward. They can be distinguished in (d) MLT vs ϕ , where ϕ is the angle between SM x-axis and \vec{v}_{2D} . In panel d, the four orthogonal directions in the polar coordinate are checked, including eastward (blue), westward (green), radially inward (red), and outward (purple). Each cross corresponds to a \vec{v}_{2D} vector. The vectors in one event are connected by gray lines. The majority of events are azimuthal (eastward/westward more often in post-/pre-midnight). The distribution of the radial events may not be statistically significant because the counts are low.

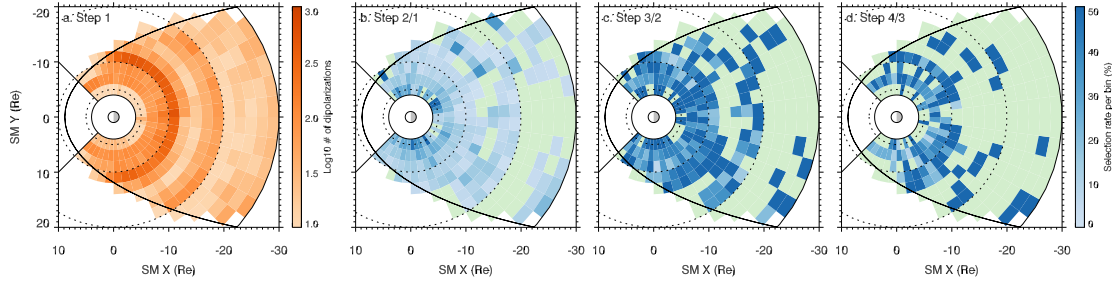


Figure 16. The distribution of dipolarizations and selection rate of each step in the event selection procedure as described in Section C. Panel a shows the distribution of all identified dipolarizations in the equatorial plane in step 1. The boundary of the region of interest (ROI) is marked by the black curves. Panel b shows the selection rate from step 1 to 2. The select rate of the green bins is 0. Similarly, panel c and d shows the selection rate from step 2 to 3 and from step 3 to 4, respectively. In panel d, the gap of dipolarization appears around midnight may suggest the propagation direction is more complicated around midnight (c.f. Section 5 for a more detailed discussion).

References

- Angelopoulos, V., Artemyev, A., Phan, T. D., & Miyashita, Y. (2020). Near-Earth magnetotail reconnection powers space storms. *Nature Physics*, *16*(3), 317–321. Retrieved from <https://doi.org/10.1038/s41567-019-0749-4> doi: 10.1038/s41567-019-0749-4
- Angelopoulos, V., Baumjohann, W., Kennel, C. F., Coroniti, F. V., Kivelson, M. G., Pellat, R., ... Paschmann, G. (1992). Bursty bulk flows in the inner central plasma sheet. *Journal of Geophysical Research: Space Physics*, *97*(A4), 4027–4039. Retrieved from <http://dx.doi.org/10.1029/91JA02701> doi: 10.1029/91JA02701
- Angelopoulos, V., Coroniti, F. V., Kennel, C. F., Kivelson, M. G., Walker, R. J., Russell, C. T., ... Harris, T. (1996). Multipoint analysis of a bursty bulk flow event on April 11, 1985. *Journal of Geophysical Research: Space Physics*, *101*(A3), 4967–4989. Retrieved from <https://agupubs.onlinelibrary.wiley.com/doi/abs/10.1029/95JA02722> doi: <https://doi.org/10.1029/95JA02722>
- Angelopoulos, V., McFadden, J. P., Larson, D., Carlson, C. W., Mende, S. B., Frey, H., ... Kepko, L. (2008). Tail Reconnection Triggering Substorm Onset. *Science*, *321*(5891), 931–935. Retrieved from <https://science.sciencemag.org/content/321/5891/931> doi: 10.1126/science.1160495
- Apatenkov, S. V., Sergeev, V. A., Kubyshkina, M. V., Nakamura, R., Baumjohann, W., Runov, A., ... Khotyaintsev, Y. (2007). Multi-spacecraft observation of plasma dipolarization/injection in the inner magnetosphere. *Annales Geophysicae*, *25*(3), 801–814. Retrieved from <https://angeo.copernicus.org/articles/25/801/2007/> doi: 10.5194/angeo-25-801-2007
- Auster, H. U., Glassmeier, K. H., Magnes, W., Aydogar, O., Baumjohann, W., Constantinescu, D., ... Wiedemann, M. (2008, dec). The THEMIS Fluxgate Magnetometer. *Space Science Reviews*, *141*(1), 235–264. Retrieved from <https://doi.org/10.1007/s11214-008-9365-9> doi: 10.1007/s11214-008-9365-9
- Baumjohann, W., Hesse, M., Kokubun, S., Mukai, T., Nagai, T., & Petrukovich, A. A. (1999). Substorm dipolarization and recovery. *Journal of Geophysical Research: Space Physics*, *104*(A11), 24995–25000. Retrieved from <https://agupubs.onlinelibrary.wiley.com/doi/abs/10.1029/1999JA900282> doi: <https://doi.org/10.1029/1999JA900282>
- Baumjohann, W., Paschmann, G., & Lühr, H. (1990). Characteristics of high-speed ion flows in the plasma sheet. *Journal of Geophysical Research: Space Physics*, *95*(A4), 3801–3809. Retrieved from <http://dx.doi.org/10.1029/JA095iA04p03801> doi: 10.1029/JA095iA04p03801
- Birn, J., Liu, J., Runov, A., Kepko, L., & Angelopoulos, V. (2019). On the Contribution of Dipolarizing Flux Bundles to the Substorm Current Wedge and to Flux and Energy Transport. *Journal of Geophysical Research: Space Physics*, *124*(7), 5408–5420. Retrieved from <https://agupubs.onlinelibrary.wiley.com/doi/abs/10.1029/2019JA026658> doi: <https://doi.org/10.1029/2019JA026658>
- Cummings, W. D., Barfield, J. N., & Coleman Jr., P. J. (1968). Magnetospheric substorms observed at the synchronous orbit. *Journal of Geophysical Research (1896-1977)*, *73*(21), 6687–6698. Retrieved from <https://agupubs.onlinelibrary.wiley.com/doi/abs/10.1029/JA073i021p06687> doi: 10.1029/JA073i021p06687
- Fu, H., Grigorenko, E. E., Gabrielse, C., Liu, C., Lu, S., Hwang, K. J., ... Chen, F. (2020). Magnetotail dipolarization fronts and particle acceleration: A review. *Science China Earth Sciences*, *63*(2), 235–256. Retrieved from <https://doi.org/10.1007/s11430-019-9551-y> doi: 10.1007/s11430-019-9551-y
- Gabrielse, C., Angelopoulos, V., Harris, C., Artemyev, A., Kepko, L., & Runov, A. (2017). Extensive electron transport and energization via multiple, localized dipolarizing flux bundles. *Journal of Geophysical Re-*

- search: *Space Physics*, 122(5), 5059–5076. Retrieved from <https://agupubs.onlinelibrary.wiley.com/doi/abs/10.1002/2017JA023981> doi: <https://doi.org/10.1002/2017JA023981>
- Huang, S. Y., Fu, H. S., Vaivads, A., Yuan, Z. G., Pang, Y., Zhou, M., ... Wang, D. D. (2015). Dawn-dusk scale of dipolarization front in the Earth's magnetotail: multi-cases study. *Astrophysics and Space Science*, 357(1), 22. Retrieved from <https://doi.org/10.1007/s10509-015-2298-3> doi: 10.1007/s10509-015-2298-3
- Kepko, L., McPherron, R. L., Amm, O., Apatenkov, S., Baumjohann, W., Birn, J., ... Sergeev, V. (2015, jul). Substorm Current Wedge Revisited. *Space Science Reviews*, 190(1), 1–46. Retrieved from <https://doi.org/10.1007/s11214-014-0124-9> doi: 10.1007/s11214-014-0124-9
- Kletzing, C. A., Kurth, W. S., Acuna, M., MacDowall, R. J., Torbert, R. B., Averkamp, T., ... Tyler, J. (2013, nov). The Electric and Magnetic Field Instrument Suite and Integrated Science (EMFISIS) on RBSP. *Space Science Reviews*, 179(1), 127–181. Retrieved from <https://doi.org/10.1007/s11214-013-9993-6> doi: 10.1007/s11214-013-9993-6
- Liou, K., Meng, C.-I., Lui, A. T. Y., Newell, P. T., & Wing, S. (2002). Magnetic dipolarization with substorm expansion onset. *Journal of Geophysical Research: Space Physics*, 107(A7), SMP 23–1–SMP 23–12. Retrieved from <https://agupubs.onlinelibrary.wiley.com/doi/abs/10.1029/2001JA000179> doi: 10.1029/2001JA000179
- Liu, J., Angelopoulos, V., Runov, A., & Zhou, X.-Z. (2013). On the current sheets surrounding dipolarizing flux bundles in the magnetotail: The case for wedgelets. *Journal of Geophysical Research: Space Physics*, 118(5), 2000–2020. Retrieved from <https://agupubs.onlinelibrary.wiley.com/doi/abs/10.1002/jgra.50092> doi: 10.1002/jgra.50092
- Liu, J., Angelopoulos, V., Zhou, X.-Z., & Runov, A. (2014). Magnetic flux transport by dipolarizing flux bundles. *Journal of Geophysical Research: Space Physics*, 119(2), 909–926. Retrieved from <https://agupubs.onlinelibrary.wiley.com/doi/abs/10.1002/2013JA019395> doi: 10.1002/2013JA019395
- Lui, A. T. Y. (1996). Current disruption in the Earth's magnetosphere: Observations and models. *Journal of Geophysical Research: Space Physics*, 101(A6), 13067–13088. Retrieved from <https://agupubs.onlinelibrary.wiley.com/doi/abs/10.1029/96JA00079> doi: 10.1029/96JA00079
- McPherron, R. L., Russell, C. T., & Aubry, M. P. (1973). Satellite studies of magnetospheric substorms on August 15, 1968: 9. Phenomenological model for substorms. *Journal of Geophysical Research (1896-1977)*, 78(16), 3131–3149. Retrieved from <https://agupubs.onlinelibrary.wiley.com/doi/abs/10.1029/JA078i016p03131> doi: 10.1029/JA078i016p03131
- Merkin, V. G., Panov, E. V., Sorathia, K. A., & Ukhorskiy, A. Y. (2019). Contribution of Bursty Bulk Flows to the Global Dipolarization of the Magnetotail During an Isolated Substorm. *Journal of Geophysical Research: Space Physics*, 124(11), 8647–8668. Retrieved from <https://agupubs.onlinelibrary.wiley.com/doi/abs/10.1029/2019JA026872> doi: <https://doi.org/10.1029/2019JA026872>
- Nagai, T. (1982). Observed magnetic substorm signatures at synchronous altitude. *Journal of Geophysical Research: Space Physics*, 87(A6), 4405–4417. Retrieved from <https://agupubs.onlinelibrary.wiley.com/doi/abs/10.1029/JA087iA06p04405> doi: 10.1029/JA087iA06p04405
- Nakamura, R., Baumjohann, W., Klecker, B., Bogdanova, Y., Balogh, A., Rème, H., ... Runov, A. (2002). Motion of the dipolarization front during a flow burst event observed by Cluster. *Geophysical Research Letters*, 29(20), 3–4. Retrieved from <https://agupubs.onlinelibrary.wiley.com/doi/abs/10.1029/2002GL015763> doi: 10.1029/2002GL015763

- Nakamura, R., Baumjohann, W., Panov, E., Petrukovich, A. A., Angelopoulos, V., Volwerk, M., ... McFadden, J. (2011). Flux transport, dipolarization, and current sheet evolution during a double-onset substorm. *Journal of Geophysical Research: Space Physics*, 116(A5). Retrieved from <https://agupubs.onlinelibrary.wiley.com/doi/abs/10.1029/2010JA015865> doi: <https://doi.org/10.1029/2010JA015865>
- Ohtani, S., Motoba, T., Gkioulidou, M., Takahashi, K., & Singer, H. J. (2018). Spatial Development of the Dipolarization Region in the Inner Magnetosphere. *Journal of Geophysical Research: Space Physics*, 123(7), 5452–5463. Retrieved from <https://agupubs.onlinelibrary.wiley.com/doi/abs/10.1029/2018JA025443> doi: 10.1029/2018JA025443
- Paschmann, G., & W. Daly, P. (2008). Multi-Spacecraft Analysis Methods Revisited. *ISSI Scientific Report (2008)*.
- Runov, A., Angelopoulos, V., Sitnov, M. I., Sergeev, V. A., Bonnell, J., McFadden, J. P., ... Auster, U. (2009). THEMIS observations of an earthward-propagating dipolarization front. *Geophysical Research Letters*, 36(14). Retrieved from <http://dx.doi.org/10.1029/2009GL038980> doi: 10.1029/2009GL038980
- Runov, A., Angelopoulos, V., Zhou, X.-Z., Zhang, X.-J., Li, S., Plaschke, F., & Bonnell, J. (2011). A THEMIS multicase study of dipolarization fronts in the magnetotail plasma sheet. *Journal of Geophysical Research: Space Physics*, 116(A5). Retrieved from <https://agupubs.onlinelibrary.wiley.com/doi/abs/10.1029/2010JA016316> doi: 10.1029/2010JA016316
- Sergeev, V. A., Sormakov, D. A., Apatenkov, S. V., Baumjohann, W., Nakamura, R., Runov, A. V., ... Nagai, T. (2006). Survey of large-amplitude flapping motions in the midtail current sheet. *Annales Geophysicae*, 24(7), 2015–2024. Retrieved from <https://hal.archives-ouvertes.fr/hal-00318134>
- Shue, J.-H., Song, P., Russell, C. T., Steinberg, J. T., Chao, J. K., Zastenker, G., ... Kawano, H. (1998). Magnetopause location under extreme solar wind conditions. *Journal of Geophysical Research: Space Physics*, 103(A8), 17691–17700. Retrieved from <https://agupubs.onlinelibrary.wiley.com/doi/abs/10.1029/98JA01103> doi: 10.1029/98JA01103
- Sigsbee, K., Slavin, J. A., Lepping, R. P., Szabo, A., Øieroset, M., Kaiser, M. L., ... Singer, H. J. (2005). Statistical and superposed epoch study of dipolarization events using data from Wind perigee passes. *Annales Geophysicae*, 23(3), 831–851. Retrieved from <https://angeo.copernicus.org/articles/23/831/2005/> doi: 10.5194/angeo-23-831-2005
- Singer, H., Matheson, L., Grubb, R., Newman, A., & Bouwer, D. (1996, oct). Monitoring space weather with the GOES magnetometers. In E. Washwell (Ed.), *Goes-8 and beyond* (Vol. 2812, pp. 299–308). doi: 10.1117/12.254077
- Torbert, R. B., Russell, C. T., Magnes, W., Ergun, R. E., Lindqvist, P.-A., LeContel, O., ... Lappalainen, K. (2016, mar). The FIELDs Instrument Suite on MMS: Scientific Objectives, Measurements, and Data Products. *Space Science Reviews*, 199(1), 105–135. Retrieved from <https://doi.org/10.1007/s11214-014-0109-8> doi: 10.1007/s11214-014-0109-8
- Tsyganenko, N. A. (1989). A magnetospheric magnetic field model with a warped tail current sheet. *Planetary and Space Science*, 37(1), 5–20. Retrieved from <http://www.sciencedirect.com/science/article/pii/0032063389900664> doi: [http://dx.doi.org/10.1016/0032-0633\(89\)90066-4](http://dx.doi.org/10.1016/0032-0633(89)90066-4)
- Ukhorskiy, A. Y., Sorathia, K. A., Merkin, V. G., Sitnov, M. I., Mitchell, D. G., & Gkioulidou, M. (2018). Ion Trapping and Acceleration at Dipolarization Fronts: High-Resolution MHD and Test-Particle Simulations. *Journal of Geophysical Research: Space Physics*, 123(7), 5580–5589. Retrieved from <https://agupubs.onlinelibrary.wiley.com/doi/abs/10.1029/2018JA025370> doi: 10.1029/2018JA025370

Figure 1.

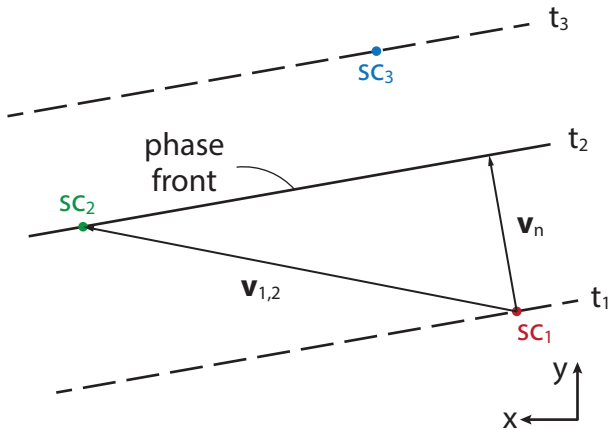
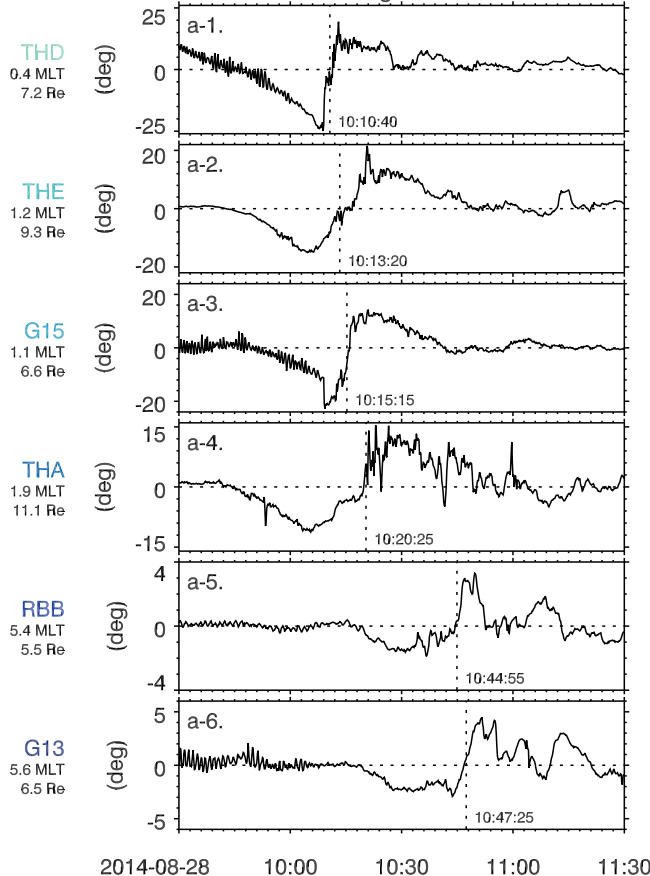


Figure 2.

Detrended tilt angle θ in absolute time

Time lag removed

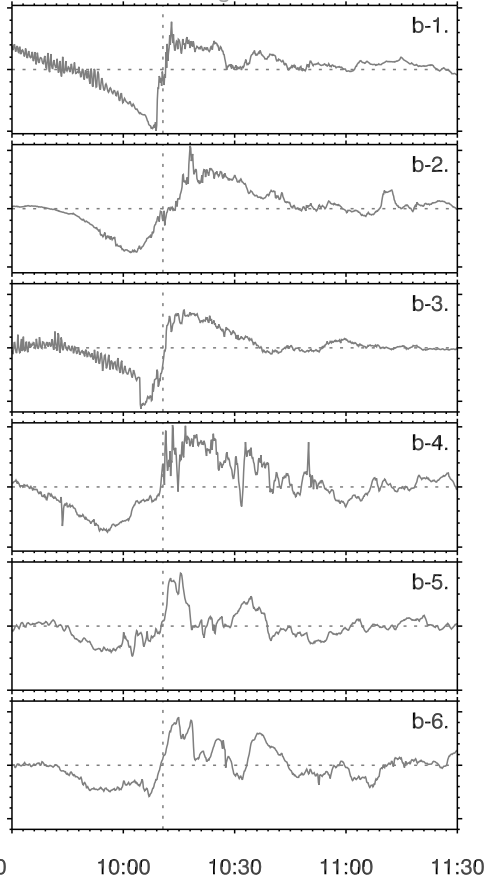


Figure 3.

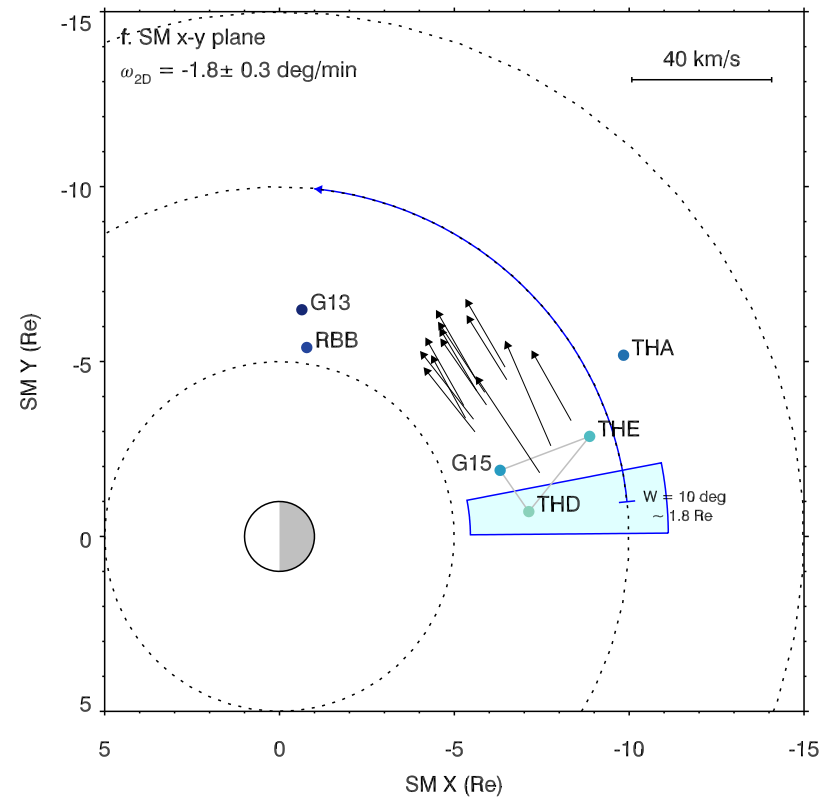
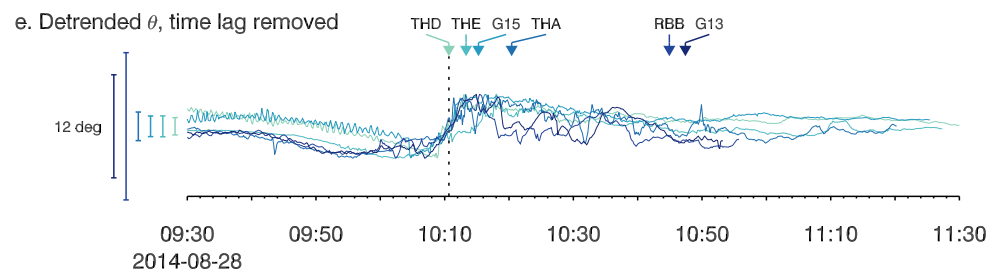
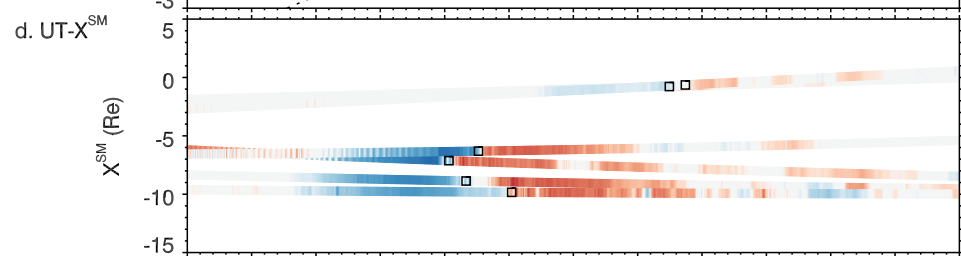
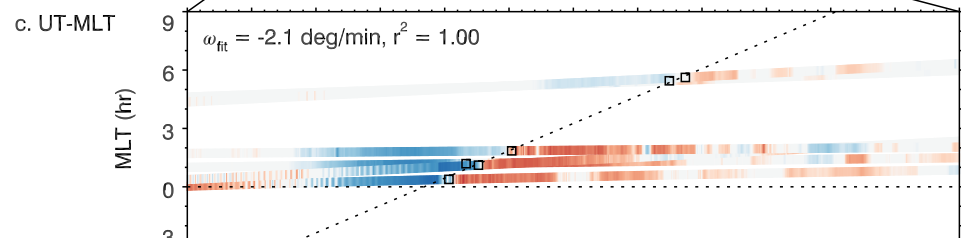
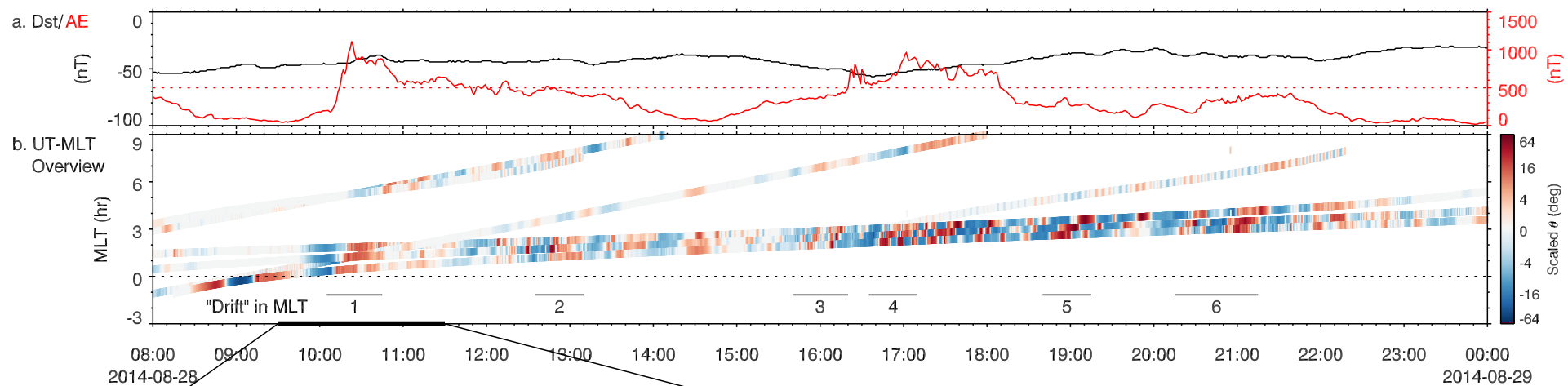


Figure 4.

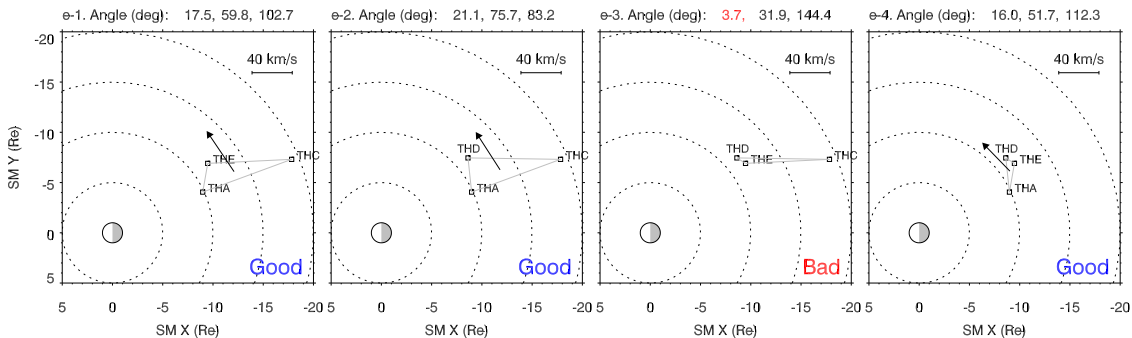
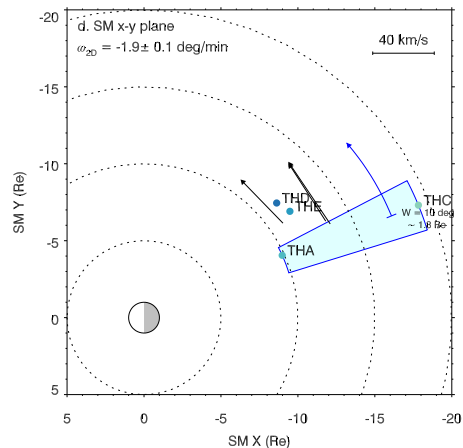
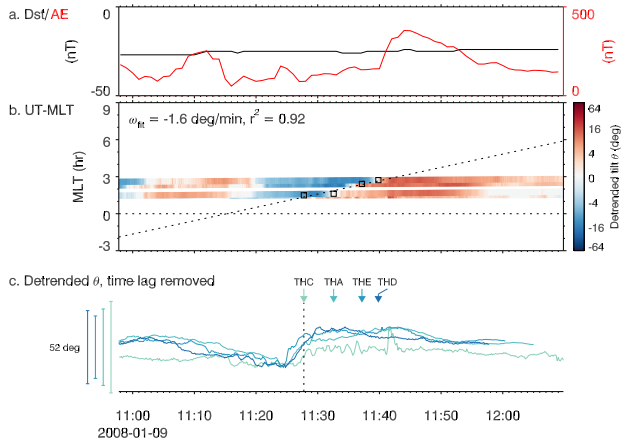


Figure 5.

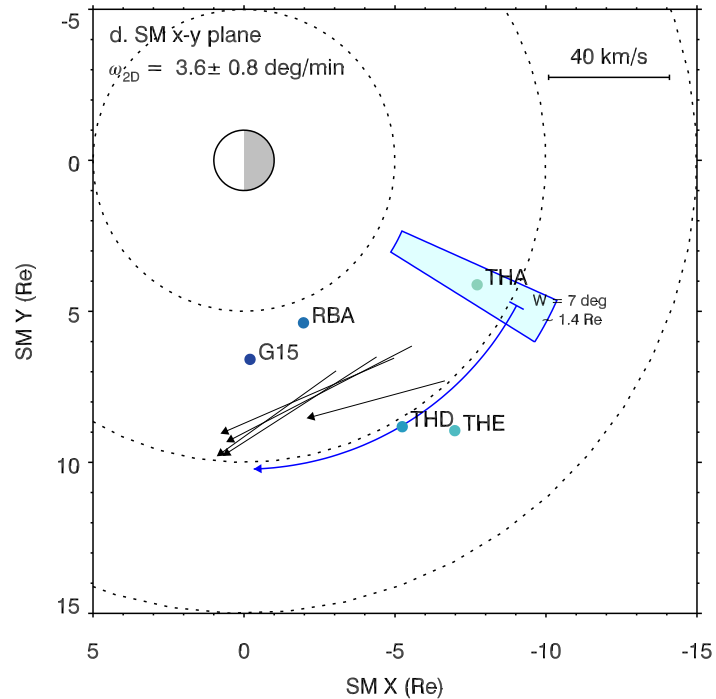
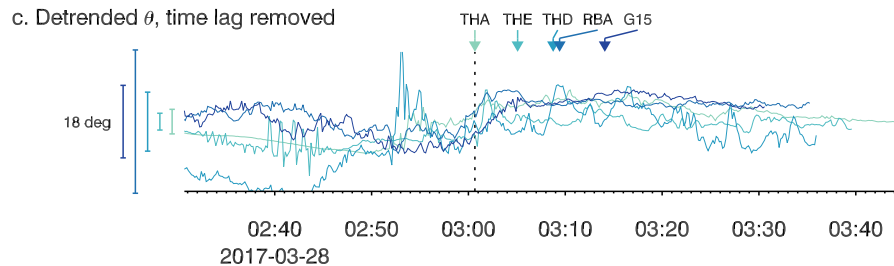
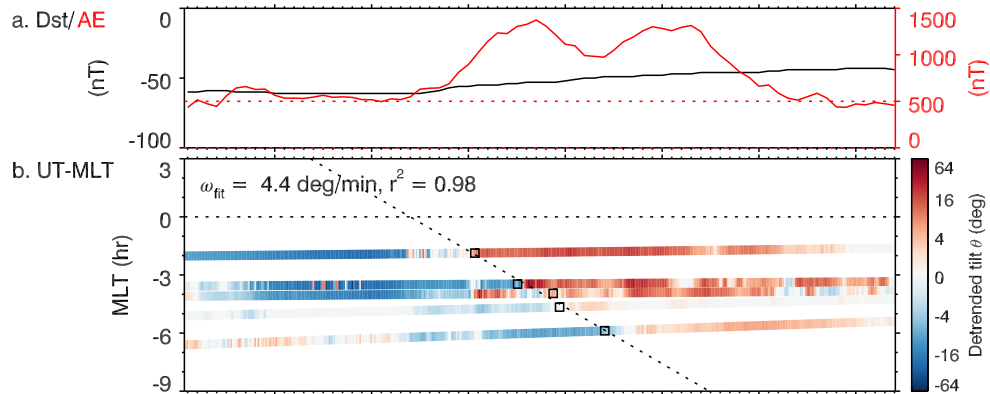


Figure 6.

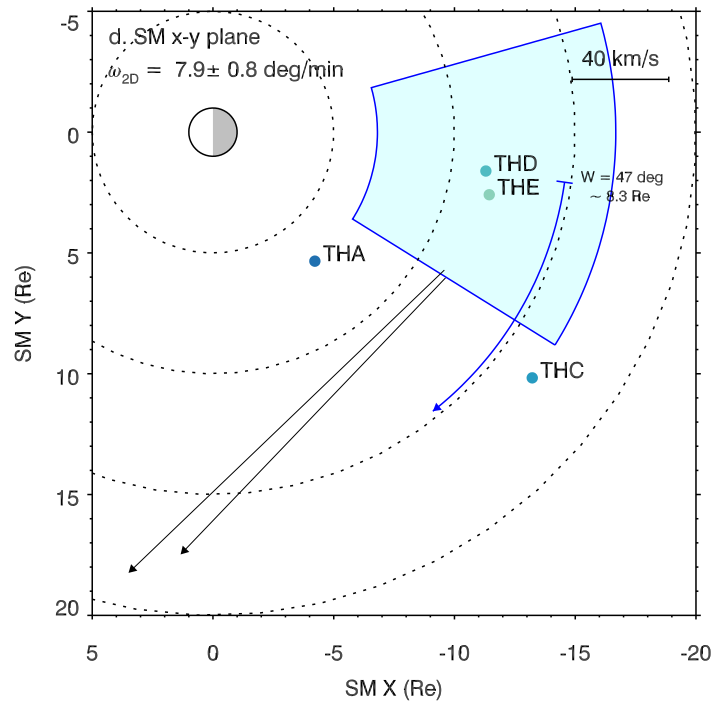
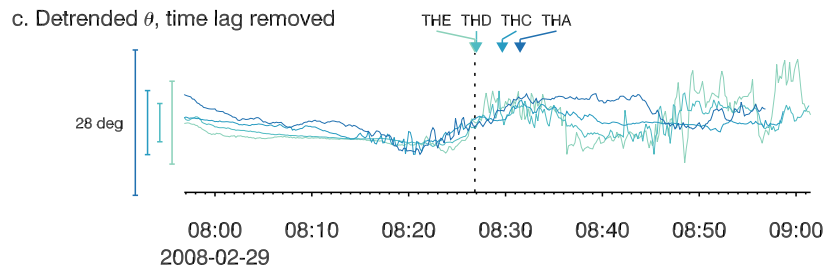
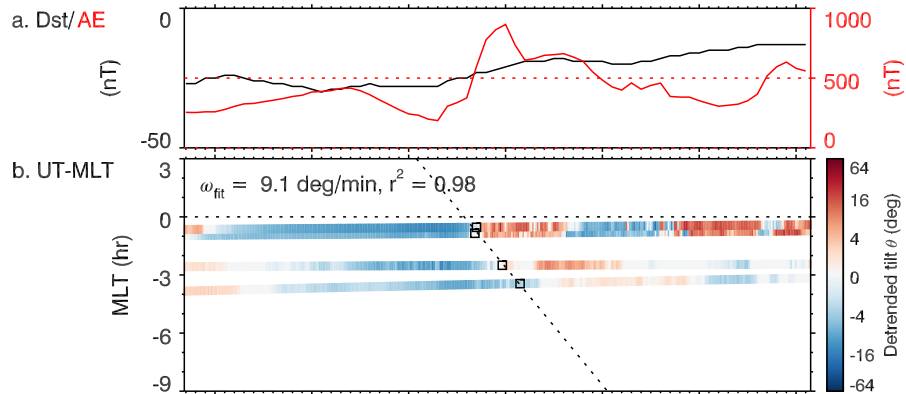


Figure 7.

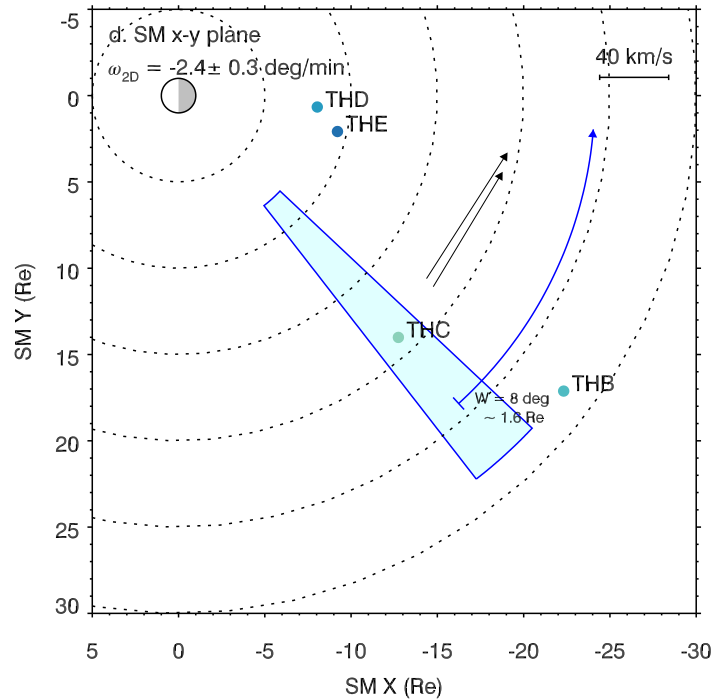
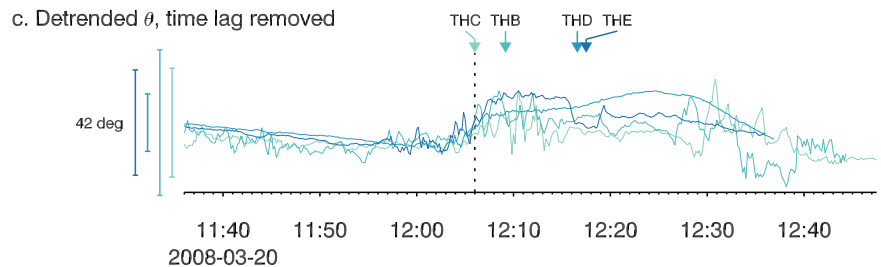
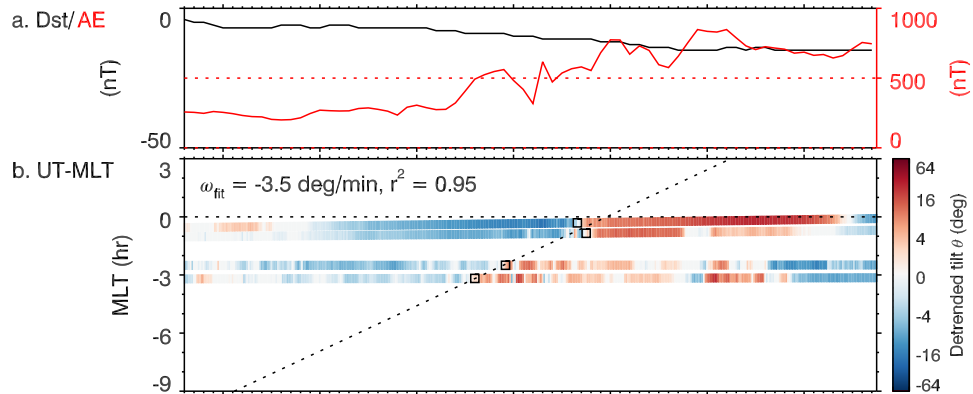


Figure 8.

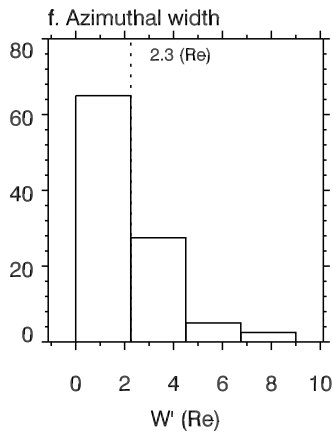
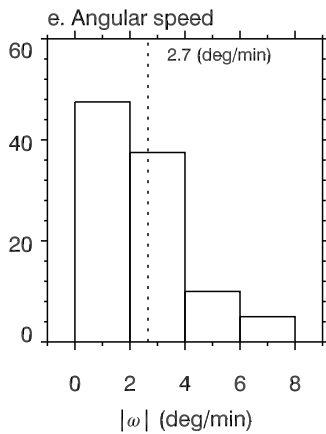
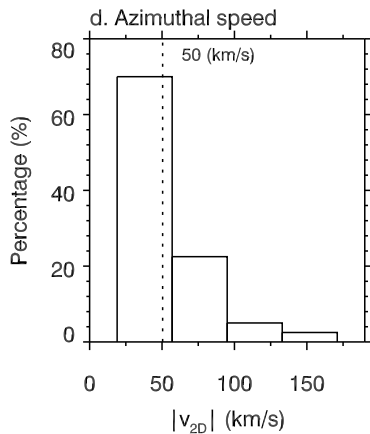
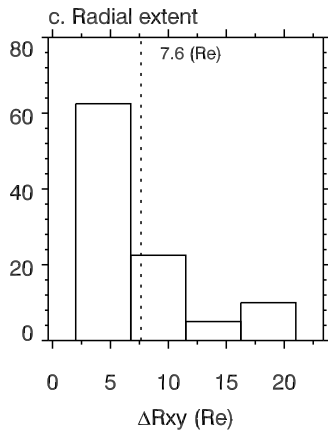
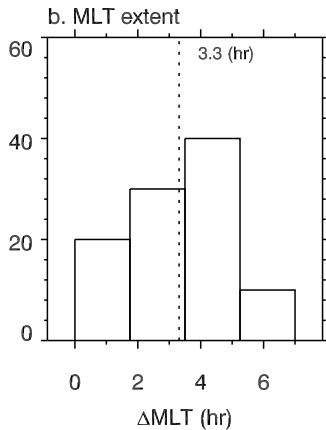
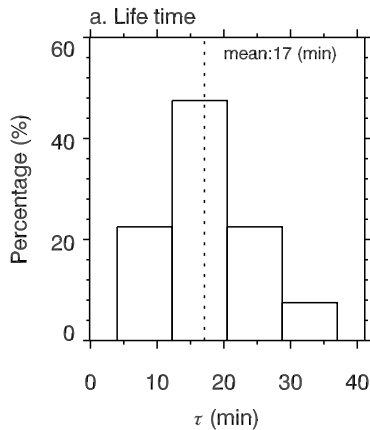


Figure 9.

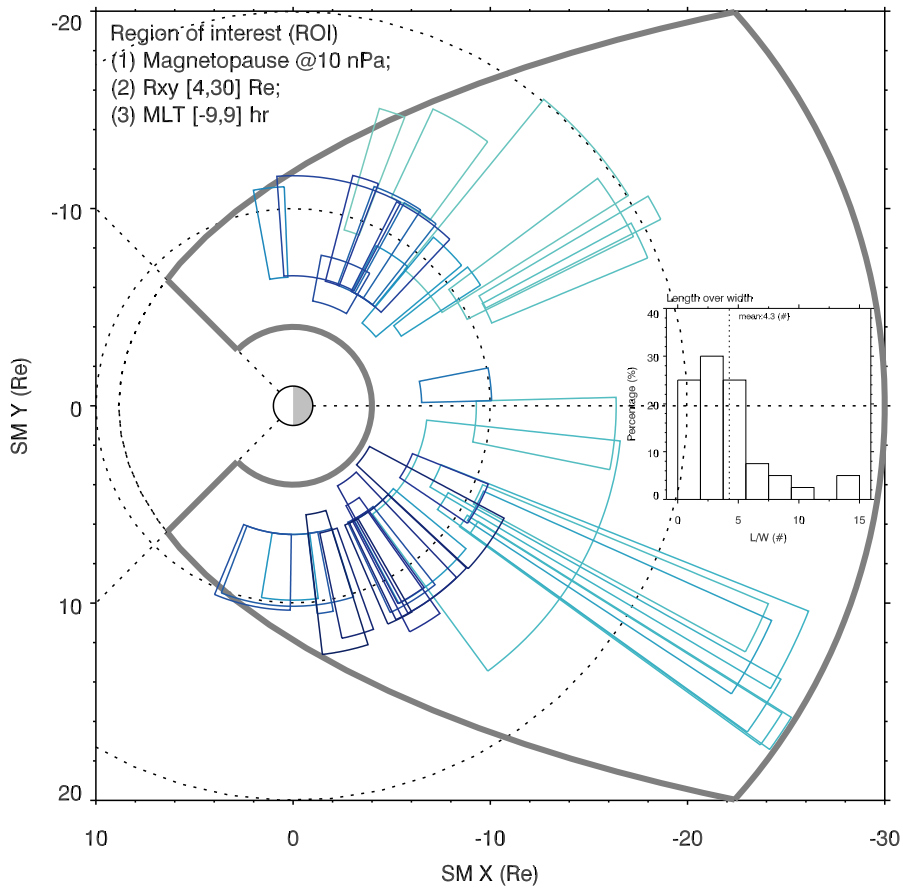


Figure 10.

Earthward: ~ 500 km/s, ~ 5 min
Azimuthal: ~ 3 deg/min, ~ 30 min

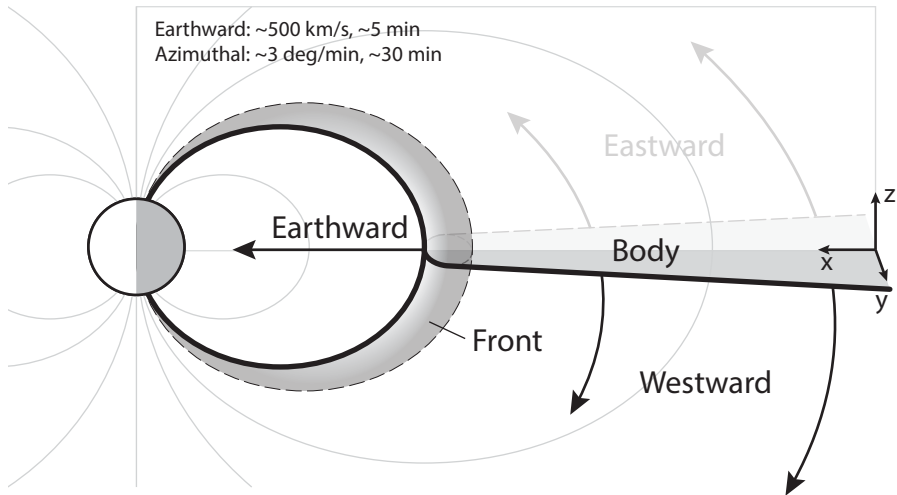


Figure 11.

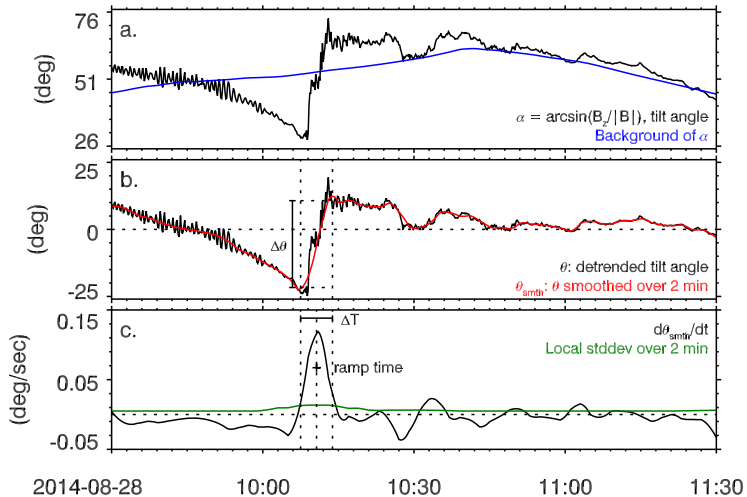


Figure 12.

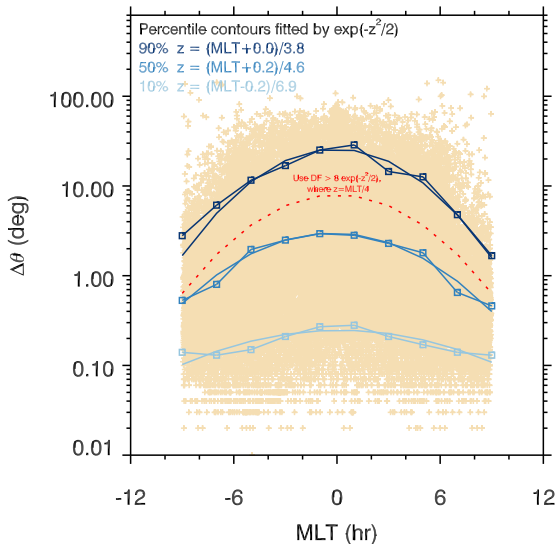


Figure 13.

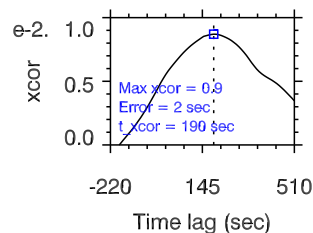
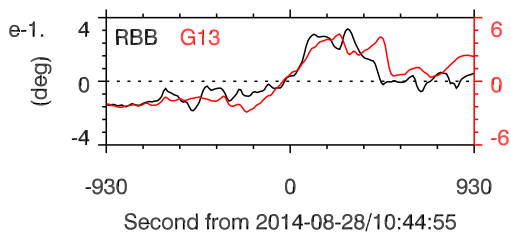
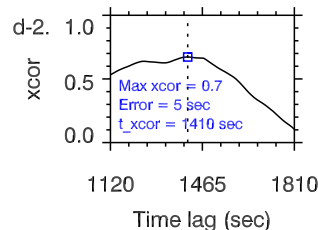
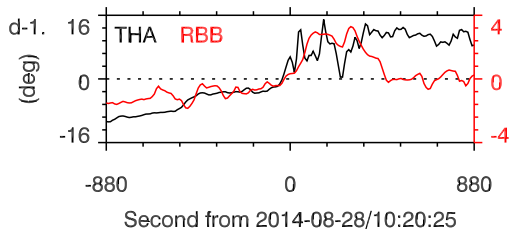
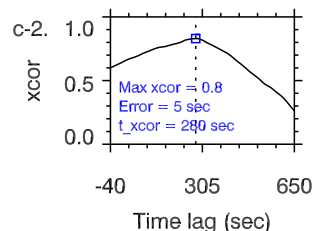
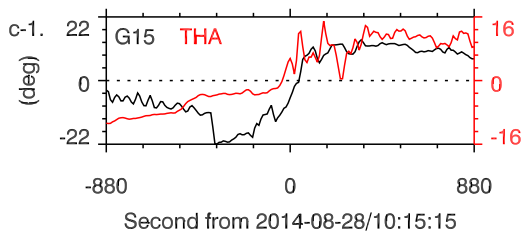
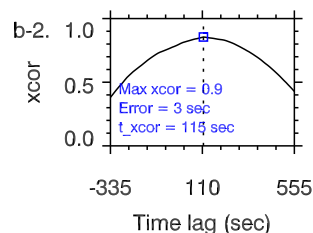
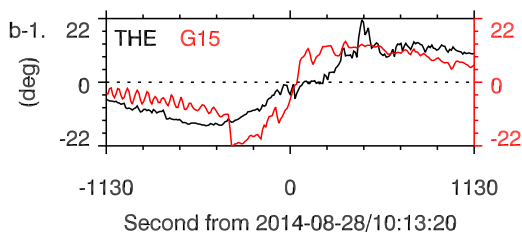
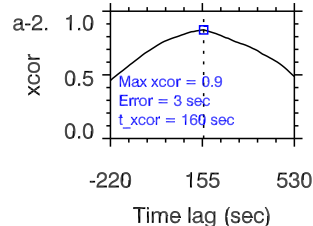
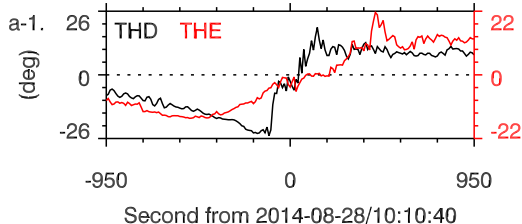


Figure 14.

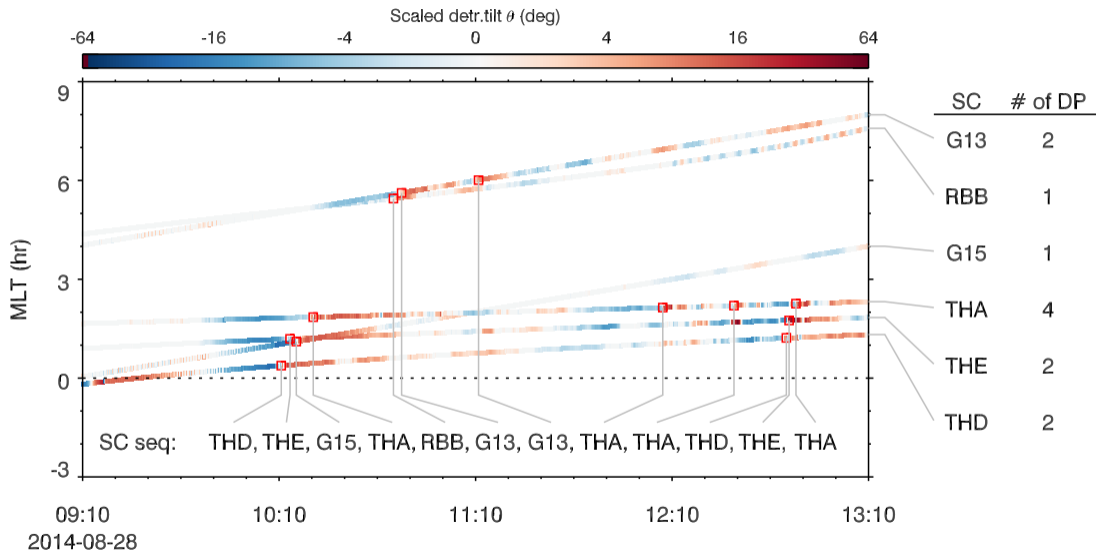
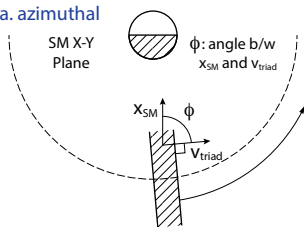
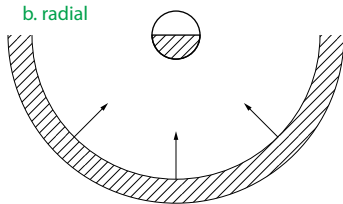


Figure 15.

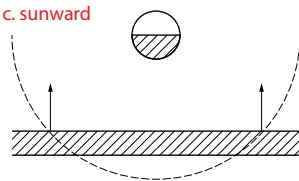
a. azimuthal



b. radial



c. sunward



d. v_{2D} direction vs MLT

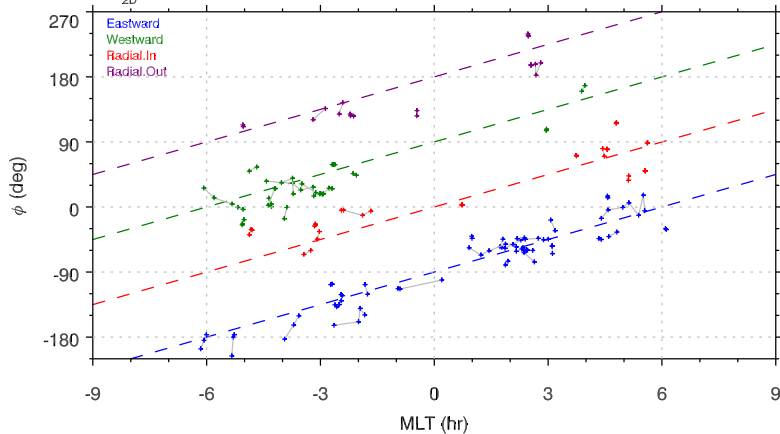


Figure 16.

